UCLouvain

epl

École polytechnique de Louvain

Encoding and manipulating two qubits inside a single Rydberg atom

Theoretical study

Author: **Brieuc VALENTIN**
Supervisor: **Matthieu GÉNÉVRIEZ**
Readers: **Sorin MELINTE, Bernard PIRAUX**
Academic year 2023–2024
Master [120] in Physical Engineering

Contents

Introduction **1**

1 Theoretical background **3**
1.1 Quantum bits and quantum gates . . . 3
1.2 Rydberg atoms . . . 7
1.2.1 Basic principles . . . 7
1.2.2 Rydberg blockade . . . 9
1.2.3 Types of Rydberg qubits . . . 12
1.3 Electronic structure of calcium Rydberg atom . . . 14
1.3.1 Calcium atom selection . . . 14
1.3.2 Electronic structure of the calcium ion . . . 14
1.3.3 Valence electrons interaction . . . 15

2 Two qubits architecture **19**
2.1 Description of the project . . . 19
2.2 Selection of electronic levels . . . 21
2.2.1 Computation of energy-level shifts . . . 21
2.2.2 Discussion of the results and determination of levels . . . 27

3 CNOT gate simulation **31**
3.1 Quantum system description . . . 31
3.1.1 Light-matter interaction . . . 31
3.1.2 Hamiltonian construction . . . 35
3.2 Light dressing . . . 38
3.3 Incoherent relaxation processes . . . 42
3.3.1 Autoionization . . . 42
3.3.2 Spontaneous emission of ion-core states . . . 44
3.3.3 Rydberg lifetime decay . . . 45
3.4 Laser pulse simulation . . . 46
3.5 Evolution of the quantum system . . . 48
3.6 Results discussion . . . 51
3.6.1 CNOT performances and fidelity . . . 51
3.6.2 Entanglement generation and Bell fidelity . . . 53

4 Qubits measurement and local gates **55**
4.1 Projective measurement 55
4.2 Single-qubit gates 60
4.2.1 Single-qubit gates fundamentals 60
4.2.2 Local Z-gate for the Rydberg qubit 61

Conclusion **64**

APPENDIX **66**

A Multiple atoms system **67**
A.1 Introduction 67
A.2 Rydberg-Rydberg interactions 67

Bibliography **72**

Abstract

This Master thesis explores an innovative two-qubit architecture within a single calcium Rydberg atom, using the electronic states of the valence electrons to encode the qubits. One qubit is encoded in levels of the ion core of a Rydberg atom, while the other utilizes Rydberg levels. The primary focus of this research is the simulation and performance analysis of a CNOT gate, which is shown to be feasible with high fidelity and efficient gate times, using the Rydberg qubit as the control and the core qubit as the target. Additionally, the study investigates an alternative architecture involving dressed states, highlighting the trade-offs between gate speed and fidelity in the presence of relaxation processes. Projective measurements and single-qubit gates on both qubits are also examined to propose a system that meets the key requirements for quantum computing. This thesis theoretically demonstrates the viability of this two-qubit architecture for quantum computing and provides a strong foundation for subsequent experimental implementations. Future directions and potential improvements are also briefly outlined, with the hope of inspiring continued research in this promising area.

Acknowledgements

This Master thesis could not have been written without the help of several people who supported me, both in my work and throughout these long months.

First, I want to express my deep thanks to my supervisor, Matthieu Génévriez, for all the time and effort he invested in my thesis. Your accessibility and the many hours you spent re-explaining physics to me in your office were invaluable. I am truly grateful for the trust you placed in me to take on this innovative project and for guiding me every step of the way. I have discovered so much about atomic physics and have grown a lot through this experience.

I also want to thank my thesis readers, Sorin Melinte and Bernard Piraux, for taking the time to read my thesis and attend my defense, helping to evaluate me in this final stage of my studies.

A big thank you to the entire NAPS team for welcoming me into their office during these months, especially to Alisée for helping me understand her thesis and for unlocking some challenging situations.

I am also grateful to the entire Porcheresse team for the years we spent studying together with good humor, from our first Christmas study session in 2019 to this final, challenging summer. These five years would not have been the same without you. A special mention goes to the Conquête team, who made this year even more successful.

Finally, I want to thank my parents, brothers, and sisters for supporting me during these last few months, and throughout all the exam periods of my engineering studies. A special thanks also to Elisabeth.

Introduction

Quantum technologies, leveraging the unique principles of quantum mechanics, have undergone rapid development in recent decades, driven by advancements in the precision of devices capable of measuring and manipulating small quantum objects. These advancements have fueled breakthroughs in various applications such as quantum computing, and quantum simulation [1].
Quantum computing promises significantly faster calculations than any classical computer can achieve today. While these computers won't entirely replace classical ones, they will be invaluable for tasks requiring immense computational power and could find applications in domains such as financial modeling, cybersecurity, artificial intelligence, and weather forecasting. In fact, quantum computers are no longer just a concept but are already part of our lives. Companies like IBM, Google, Amazon, and Microsoft sell quantum machines and invest heavily in this technology. The total market value for quantum computing was 1.3 billion USD in 2024 and is expected to grow to 5.3 billion USD by 2029 [2].
Besides quantum computing, quantum simulators [3] have emerged as powerful tools for studying complex quantum systems that are difficult to simulate with classical computers. Quantum simulators leverage the principles of quantum mechanics to model and solve specific problems in areas like condensed matter physics [4], quantum chemistry [5], and high-energy physics [6]. While many of these problems remain unsolvable for classical simulators, quantum simulators may provide solutions, advancing our understanding of fundamental physics and enabling the development of new technologies.

In quantum technologies, information is represented by physical states that are sufficiently microscopic and isolated, ensuring they obey the laws of quantum mechanics. These states are known as "quantum bits," or qubits. The main advantage of quantum technologies over classical ones lies in the principle of superposition of states. In quantum systems, different states can exist simultaneously, and like physical waves, quantum states can be combined, allowing for interferometry. A quantum computer with n qubits can be in a superposition of 2^n states, ranging from $|00\ldots0\rangle$ to $|11\ldots1\rangle$, whereas a classical computer with n bits can only exist

in one of these 2^n states at any given time. This capability enables the simultaneous computation of multiple possibilities, which is incredibly powerful for tackling large and complex problems that would be infeasible for classical computers. Additionally, it allows for the realistic simulation of quantum systems, accurately mimicking their behavior.

In order to perform quantum computing or simulation, it is essential to have qubits that can effectively resist decoherence, a phenomenon in which information is lost due to external interactions within the quantum system. Equally important is the speed at which operations can be performed on these qubits, as it is necessary to complete a sufficient number of operations before the quantum system transitions to different states. The main challenge lies in creating qubits that satisfy both of these criteria, as outlined by DiVincenzo in his well-known criteria for quantum computing [7]. Currently, there are various techniques for constructing qubits, each with its own advantages and disadvantages.

In this thesis, we explore a technique for creating qubits within a single calcium atom in a Rydberg state. Rydberg technologies, which leverage the unique properties of these highly excited atoms, are currently viewed as highly promising for future applications [8, 9]. The main idea of this thesis is to develop an architecture that includes two qubits within a single atom, a concept that has not yet been realized. For this purpose, an alkaline-earth atom with two valence electrons has been chosen. The qubits are encoded in various electronic states of a calcium atom, with one of the valence electrons occupying a Rydberg state.
Chapter 1 provides the theoretical background necessary to understand the field. Chapter 2 details the process of determining the appropriate energy levels for qubit encoding. Chapter 3 presents simulations of a quantum two-qubit gate, while Chapter 4 discusses qubit measurement and single-qubit gate. Although no experimental work was conducted in this study, simulations were performed to closely replicate real-world conditions, assess the feasibility of the proposed setup, and predict performance outcomes. This work aims to lay the groundwork for future experimental implementations.

Chapter 1

Theoretical background

1.1 Quantum bits and quantum gates

A bit is the most fundamental unit of information in classical computing. It can be represented by any system capable of assuming two distinct states, which are typically denoted as 0 and 1, though alternative representations such as true/false, yes/no, on/off, or +/− are also common. When this two-state system is designed according to the principles of quantum mechanics, it is referred to as a qubit or quantum bit.

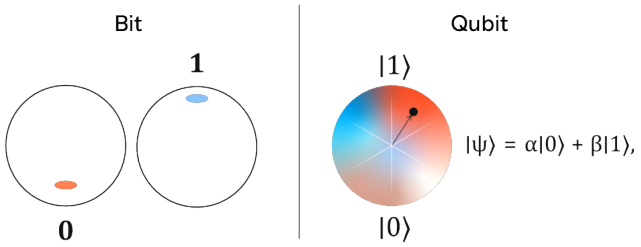

Figure 1.1 – Bit and qubit illustrated, from [10].

The quantum nature of a qubit allows it to exist in a superposition of multiple states simultaneously, a property that greatly enhances computational speed and efficiency. However, this same quantum nature also introduces several challenges. Qubits are notoriously difficult to manipulate, highly sensitive to environment interference, prone to decoherence (where quantum information is lost), and their state measurement can be problematic. These issues present significant obstacles in the development and practical implementation of quantum computing.
To assess the quality of qubits, and quantum information processing system associated with them, DiVincenzo outlined essential criteria for constructing quantum

computers in 2002, which are now widely regarded as the standard in the field [7]. These criteria are developed as follows:

1. **Well-characterized and scalable qubits:** It is essential to engineer natural quantum systems into functional qubits and to scale these systems effectively.
2. **Qubit initialization:** Qubits must be consistently initialized in the same state, within a narrow error margin.
3. **Long coherence times:** Qubits should maintain their coherence long enough to perform necessary operations, despite environmental interactions.
4. **Universal set of gates:** A complete set of quantum gates, including single- and two-qubit gates, is required to execute quantum operations.
5. **Measurement of individual qubits:** Accurate measurement of specific qubit states is crucial.

To better understand the behavior of qubits, it is important to understand certain quantum principles inherent to them. These principles will be briefly explained in the following section.

Entanglement

One counter-intuitive phenomenon in quantum physics is entanglement. When two (or more) particles are in certain superposition states and are arranged such that their states are inseparable, they are said to be in an entangled state. In this configuration, the state of one particle can be determined based on the state of the other, regardless of the distance between them, without any direct interaction. Einstein famously referred to this as "spooky action at a distance." Since then, significant research has been conducted on this phenomenon, and it was experimentally demonstrated long ago [11].

Decoherence

Decoherence describes the process by which a quantum system loses its coherence, transitioning towards behavior that can be explained by classical mechanics. It involves the wavefunction of quantum particles (see Figure 1.1), a mathematical function representing their quantum state and providing a probabilistic interpretation-collapsing irreversibly into one of its definite states. This represents the irreversible loss of quantum information to the environment. Decoherence is triggered by interactions with external factors, such as a thermal bath or

electromagnetic fields, which perturb the components of the quantum system. This spontaneous interaction with the environment explains why maintaining quantum states in real-world conditions is so challenging.

Measurement

In classical systems, measuring the state of a bit is straightforward. In contrast, in quantum systems, measuring a qubit perturbs its wavefunction, forcing it, in the typical case of a projective measurement, to collapse into a definite state (one of the basis states). This process, related to decoherence, is critical and irreversible, permanently erasing the qubit's superposed state and the information it held. Consequently, quantum measurements are inherently probabilistic, with repeated measurements aligning with the established probabilities. Furthermore, this characteristic necessitates precise control and isolation of quantum systems during experiments to limit unintentional decoherence and measurement errors. This need for precision highlights the delicate balance required in quantum experimentation and computation.

Main qubits types

As previously mentioned, there are various types of qubits, and the debate continues over which type offers the best performance. A common characteristic among these systems is that they must be cooled to extremely low temperatures to facilitate their manipulation and preservation while minimizing decoherence. These qubits can be categorized based on their underlying physical principles. The key types will be explained below:

1. **Superconducting qubits** are among the most widely-used models in quantum computing due to their scalability and high-designability [12]. Basically, a superconducting qubit is a circuit loop that includes Josephson junctions and allows an electrical current to travel around it with no resistance when cooled below a critical temperature [13]. The current consists of 'Cooper pairs', electron pairs that occur uniquely in these superconductive conditions. These circuits are quantized, enabling them to exist in multiple quantum states simultaneously. This property is key to quantum computing, allowing for the control and measurement of qubit states through the application of microwave or magnetic flux pulses .

2. **Trapped ion** quantum computers are based on ions (electrically charged atom) trapped and stored in space thanks to an electromagnetic field [14].

Quantum information is stored in electronic states of these ions, and transfer of population can be induced thanks to lasers coupling different states. We can distinguish two dominants ways to get qubits in an ion trap: two ground states hyperfine levels or one ground state and one excited state. The main difference between these setups here is the decoherence time which is longer for ground state hyperfine levels than for ground-excited electronic levels. The frequency of laser used to induce transitions is also very different because of the energy difference being far smaller between 2 hyperfine levels. To initialize ion-trapped qubits, we use optical pumping to populate the right levels, a process using lasers to couple states and induce transition. Other lasers are also used to measure the state of these qubits

3. **Neutral atom** quantum devices share some basic similarities with trapped ions, as they both use the electronic levels of atoms to encode qubit states. However, the atoms used in neutral atom devices are electrically neutral. Since neutral atoms do not experience electrical repulsion like ions, they face fewer scalability issues. Instead of using electromagnetic fields to trap ions, optical tweezers are employed to trap neutral atoms [15]. When excited to a Rydberg state, these qubits can leverage Rydberg properties, allowing them to interact over long distances through van der Waals interactions[9].

Quantum gates

Logic gates are fundamental components of all computing systems, performing essential operations that change the states of bits to enable computation. Traditional computers utilize standard gates such as the 'NOR' gate, a single-bit gate, and the 'AND' and 'OR' gates, which are two-bit gates that combine both input bits to produce a single output bit. A significant theorem in computer science, proposed by Alan Turing in 1936 [16], asserts that any algorithm can be constructed using a minimal set of logic gates known as a "universal gate set."
Quantum computing adheres to a similar principle but operates with different types of gates. Quantum gates range from single-qubit gates, which affect individual qubits, to multi-qubit gates, which can conditionally alter the states of multiple qubits based on the states of others. One notable multi-qubit gate is the controlled-NOT (CNOT) gate, which is essential for creating quantum entanglement among qubits. The CNOT gate, in conjunction with single-qubit gates, forms a universal quantum gate set, sufficient to implement any quantum algorithm. Therefore, the ability to implement and control such gates is crucial for advancing quantum computing technology. This explains why the construction of a robust and reliable CNOT gate has been a primary focus of this thesis.

1.2 Rydberg atoms

In this work, the atom used to encode two qubits must have one of its two valence electrons in a Rydberg state. Therefore, some information about these particular atoms will be explained in this section.

1.2.1 Basic principles

Rydberg atoms are highly excited atoms characterized by having at least one electron in a Rydberg electronic state, indicated by a high principal quantum number n, which typically ranges from ten to several hundred. Due to the considerable distance with the atomic core, which contains all other charges, and the Rydberg electron, the latter effectively experiences a +1 charge from the core. As a result, it can be accurately modeled by a hydrogen-like model and is often described by its quantum numbers n and ℓ. However, this model sometimes requires correction, particularly when the Rydberg electron's orbital comes close to the core; it can penetrate the region where the other electrons reside, leading to small energy shifts and phase shifts in the long-range wavefunction. This effect is more pronounced when the orbital quantum number ℓ is small. In such cases, the binding energy $W_{n\ell}$ of this electronic level should include a correction term $\delta_{n\ell}$ to the hydrogenic model:

$$W_{n\ell} = I_0 - \frac{R_y}{(n - \delta_\ell)^2}, \tag{1.1}$$

where I_0 is the ionization energy, and δ_ℓ is the quantum defect, a value that describes the deviation of an atom from the mathematically perfect hydrogen atom. The quantum defect becomes very small for $\ell > 3$ in heavy alkali atoms. R_y is the Rydberg constant, with $2R_y = 1$ a.u.
When the orbital quantum number reaches its highest value $\ell = n - 1$, and the magnetic quantum number m_ℓ equals its maximum $|m_\ell| = \ell$, the atom is in a so-called *circular state* [17].

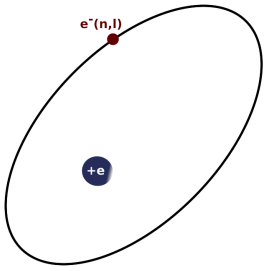

Figure 1.2 – Classical schematic of a Rydberg atom, illustrating the Rydberg electron (in brown) and the ion core (in blue). The large distance between the electron and the core emphasizes the hydrogen-like nature of the system.

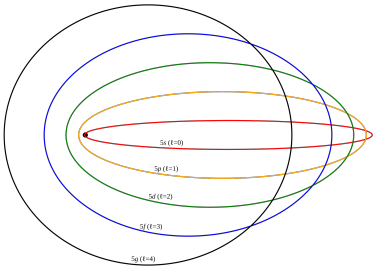

Figure 1.3 – Classical schematic of various orbitals for $n = 5$, showing how core penetration decreases as the orbital quantum number ℓ increases.

Rydberg atoms are of significant interest to researchers due to their exaggerated properties, which arise from their large quantum numbers. The Rydberg electron occupies a large, loosely bound orbital, causing these atoms to exhibit properties that are remarkably enhanced compared to those in the ground state. Many of these properties scale with the principal quantum number n (more precisely, with the effective principal quantum number $n^* = n - \delta_{n\ell}$). The table below highlights several properties that vary with n, along with the corresponding power law relationships.

Table 1.1 – Scaling law with n, the principal quantum number, for the listed properties of Rydberg atoms [18].

Properties	Notation	β (scaling n^β)
Orbit size	$\langle r \rangle$	2
Binding energy	E_n	-2
Radiative lifetime	τ_r	3
Dipole matrix element	$\langle n\ell \vert er \vert n\ell + 1 \rangle$	2
van der Waals interaction	$\langle n\ell \vert \hat{V} \vert n'\ell' \rangle$	11

- The orbital size, expressed as the average orbital radius, scales as $\propto n^2$, following the formula:

$$\overline{r} = \frac{1}{2Z}(3n^2 - \ell(\ell+1)), \tag{1.2}$$

This size can reach values as large as 1 mm (for the highest observed, with $n = 1200$ [19]), approximately the width of a human hair, surpassing the size of viruses and bacteria. Typically, with $n = 50$ and $\ell = 0$, a Rydberg atom will have a size close to 0.5 μm.

- The binding energy of Rydberg atoms scales with n^{-2}, as shown in Eq. (1.1), generating Rydberg series that converge to the ionization threshold.

- Rydberg states have very long radiative lifetimes, typically around 100 μs for $n = 50$, which exhibit a dependence on n^3 for low ℓ. The radiative lifetime is the inverse of the sum of Einstein coefficients $A_{n'\ell',n\ell}$, given by [18]:

$$A_{n'\ell',n\ell} = \frac{4e^2\omega^3_{n'\ell',n\ell}}{3\hbar c^3}\frac{\ell_{\max}}{2\ell+1}\left|\langle n'\ell'|r|n\ell\rangle\right|^2, \tag{1.3}$$

  where $\ell_{\max}$ is the larger of ℓ and ℓ'. The dependence on n^3 can be found in the norm of the square of the dipole matrix element shown in Equation (1.3). Briefly, in the limit of high n, the A value depends only on the radial matrix element between the Rydberg state and the low-lying states (due to the dependence on $\omega^3_{n'\ell',n\ell}$, which emphasizes high energy differences). Furthermore, only the part of the Rydberg state wavefunction that spatially overlaps with the wavefunction of the low-lying state contributes to the matrix element. As a result, the squared radial matrix exhibits an n^3 instead of the expected n^4 scaling.

- For neighboring Rydberg states, the dipole matrix element $\langle n,\ell|\, r\,|n,\ell-1\rangle$ associated with dipole transitions can be large and scales as $\propto n^2$.

- The van der Waals interaction between two Rydberg states of neighboring atoms exhibits a very strong dependence, $\propto n^{11}$. This strong interaction is a natural consequence of the large dipole moment featured by Rydberg states and is explained in details in the Appendix A.

1.2.2 Rydberg blockade

The strong interaction energy exhibited between two Rydberg atoms led to the discovery of the "Rydberg blockade" [20], a phenomenon now widely used in quantum technologies [9]. The interaction potential between two Rydberg atoms scales as $U_{\text{vdW}} = C_6/R^6$, where $C_6 \propto n^{11}$. The concept of the Rydberg blockade will be described in the following section.

To understand the Rydberg blockade, let us consider two atoms separated by a distance R such that they are in the van der Waals interaction regime. Depending on the excitation level of their valence electrons, these atoms can either be in the ground state $|g\rangle$ or in the Rydberg state $|r\rangle$. These two-level systems can thus occupy one of four possible states: $|gg\rangle$, $|gr\rangle$, $|rg\rangle$, or $|rr\rangle$. Due to the strong van der Waals interaction between two Rydberg atoms, the $|rr\rangle$ state is shifted by a significant amount of energy compared to the case where the atoms are infinitely far apart.
Assuming the two atoms are identical, a laser tuned to the resonance of the $|g\rangle \leftrightarrow |r\rangle$ transition can excite the system from the $|gg\rangle$ state to the $|rg\rangle$ or $|gr\rangle$ states. Specifically, the two atoms become entangled, resulting in a superposition state:

$$|\psi_+\rangle = \frac{1}{\sqrt{2}}(|rg\rangle + |gr\rangle). \tag{1.4}$$

Starting from the $|gg\rangle$ state, the system undergoes collective Rabi oscillations with a Rabi frequency of $\sqrt{2}\Omega$, where Ω is the Rabi frequency for the transition $|g\rangle \leftrightarrow |r\rangle$.
From the $|gr\rangle$, $|rg\rangle$, or $|\psi_+\rangle$ states, the same laser could, in principle, excite the system to the $|rr\rangle$ state. However, due to the energy shift U_{vdW} caused by the strong Rydberg-Rydberg interaction, the laser is no longer resonant with the $|rr\rangle$ transition. This is the Rydberg blockade where the excitation of one atom effectively prevents the excitation of the other.

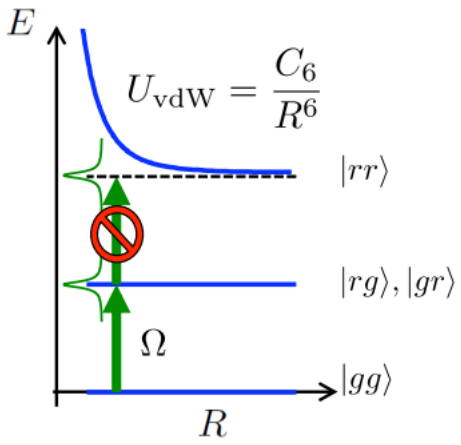

Figure 1.4 – Rydberg blockade illustration: a laser pulse associated with the Rabi frequency Ω is resonant for the transition $|gg\rangle$ to $|rg\rangle$ but not for the transition $|rg\rangle$ (or $|gr\rangle$) to $|rr\rangle$. Illustration from [21].

Since U_{vdW} decreases with R^6, the blockade mechanism only occurs if the two

atoms are within a region known as the "blockaded sphere," characterized by a radius R_b. This radius is determined by the bandwidth of the excitation source:

$$\hbar \Delta\nu = \frac{C_6}{R_b^6}, \tag{1.5}$$

where, in the case of laser excitation, $\Delta\nu$ is the laser's linewidth.

In quantum information, it is possible to leverage the surpising properties of the Rydberg blockade to build controlled interactions between qubits, and to create entanglement such as with controlled-NOT gates (CNOT)[22].

The mechanism to create a CNOT gate with the Rydberg blockade is illustrated in Figure 1.5. We have two atoms, close enough to be within the blockaded sphere, called the control and the target atoms, respectively. The controlled phase gate C_Z can be implemented using three laser pulses on these two atoms. These atoms can be in states $|0\rangle$ or $|1\rangle$, with the $|1\rangle$ state being coupled to a Rydberg state $|r\rangle$. At the start, the atoms can be in any state. A π pulse ($\Omega\tau = \pi$) is first applied to the control atom, followed by a 2π pulse on the target atom, and finally, another π pulse on the control atom. This sequence will produce a phase shift on the target atom, but only if the control atom was initially in state $|1\rangle$.

Let us examine this process in detail: If the control atom is in state $|1\rangle_c$, the first π pulse excites it to the Rydberg state $|r\rangle_c$. Due to the Rydberg blockade, the strong interaction between the Rydberg states of the two atoms detunes the excitation of the target atom for the 2π pulse so that it is blocked and leaves its state unchanged as $|1\rangle_t \rightarrow |1\rangle_t$.
However, when the control atom is in state $|0\rangle_c$, the first π pulse cannot excite it to the Rydberg state $|r\rangle_c$, then the 2π pulse on the target atom induces a phase shift as it undergoes excitation and deexcitation to the Rydberg state $|r\rangle_t$, resulting in $|1\rangle_t \rightarrow -|1\rangle_t$. The final π pulse then returns the control atom to its original state.

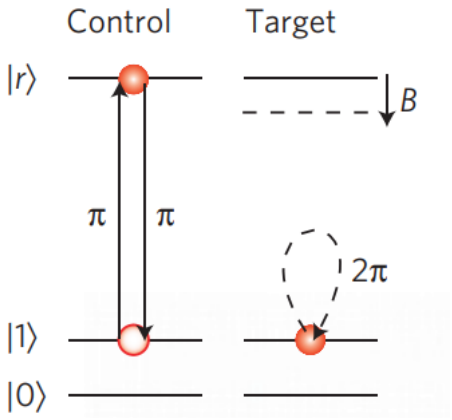

Figure 1.5 – Control and target atom with their three levels represented, the $|1\rangle$ state is coupled to a Rydberg state $|r\rangle$. When the control atom is in state $|1\rangle_c$, the strong van der Waals interaction $|r\rangle_c \leftrightarrow |r\rangle_t$ causes an energy level shift **B** that detunes the excitation of the target atom, preventing the excitation. Illustration from [23].

At the end of this process, we find the so-called C_Z phase gate which in matrix representation is:

$$C_Z = \begin{pmatrix} 1 & 0 & 0 & 0 \\ 0 & -1 & 0 & 0 \\ 0 & 0 & -1 & 0 \\ 0 & 0 & 0 & -1 \end{pmatrix}. \tag{1.6}$$

This gate can easily be converted into a CNOT gate by adding a $\pi/2$ pulse between $|0\rangle_t \leftrightarrow |1\rangle_t$ on the target atom before and after the C_Z gate. This whole sequence has been demonstrated in [22].
The gate concept presented in Chapter 3 also arises from energy shifts between electronic levels; however, in this case, they are caused by Coulomb interactions between the two valence electrons of the same atom instead of van der Waals interactions between two atoms.

1.2.3 Types of Rydberg qubits

The unique properties of Rydberg atoms have led to the development of various types of qubits that leverage these properties. These qubits can be classified into three main types, each distinguished by the specific electronic levels that constitute the qubits. It involves different characteristic energy scales, and therefore different ways to manipulate the states.

Ground-Ground (gg) qubits

Qubits are encoded in two low-energy states $|g\rangle$, such as the ground state and an excited metastable state, or two hyperfine levels of the electronic ground state. Their main advantage lies in their performance in terms of decoherence time, thanks to their long lifetime. The energy splitting between these levels typically ranges from approximately 1 to 10 GHz for hyperfine levels and optical frequencies for ground-metastable states [9]. Ground-ground qubits interact significantly less than Rydberg-ground (rg) and Rydberg-Rydberg (rr) qubits, so ground states are sometimes admixed with Rydberg levels or momentarily excited to enhance interaction strength.

Rydberg-Ground (rg) qubits

The basis states for this type of qubit consist of a weakly interacting level $|g\rangle = |0\rangle$, typically the ground state of the atom or an excited metastable state, and a strongly interacting level $|r\rangle = |1\rangle$ with a high principal quantum number n. The energy difference between these states is around 1000 THz, depending on the atom and n, necessitating the use of an ultraviolet laser to manipulate the qubits. The lifetime of these Rydberg-ground qubits is limited by the decay of the Rydberg states due to spontaneous emission and black-body radiation; for $n = 50$, it typically scales as $\tau = 100\,\mu$s [9]. The interaction between two Rydberg-ground qubits follows the van der Waals regime, $U_{\text{vdW}} = -C_6/R^6\,|11\rangle\langle 11|$. This type of qubit is currently at the forefront of quantum technology, enabling fast entangling operations in less than 100 ns.

Rydberg-Rydberg (rr) qubits

In this type of qubit, the two basis levels $|0\rangle$ and $|1\rangle$ are encoded in Rydberg states, providing significant flexibility in tuning interactions. The interaction between Rydberg states can scale as $\propto C_6/R^6$ or as $\propto C_3/R^3$ for short-range interactions and Förster resonance (Appendix A). Generally, the interaction is strongest for similar principal and orbital quantum numbers, specifically $\delta\ell = 0, 1, 2$ and $\delta n = 0, 1$, corresponding to energy splittings in the range of 10-60 GHz [9]. Manipulation of Rydberg states $|0\rangle \leftrightarrow |1\rangle$ is achieved through microwaves. However, addressing individual qubits poses challenges due to the large wavelength (approximately 1-1000 mm) and the proximity of atoms (approximately 10 μm). As with Rydberg-ground qubits, the coherence time is limited by the decay of Rydberg states, with a typical lifetime of approximately 100 μs. However, this lifetime can be enhanced up to several ms for circular states [24].

1.3 Electronic structure of calcium Rydberg atom

The content in Section 1.3 is primarily based on the work of Alisée Bouillon's thesis [25], "Theory of Rydberg-Atom Laser Cooling by Isolated Core Excitation". This section has been summarized to explain the main concepts of the electronic structure of calcium Rydberg atom. This work has been crucial in determining the interactions between the valence electrons of calcium Rydberg atom. For a more comprehensive explanation, her thesis is recommended.

1.3.1 Calcium atom selection

Calcium, a member of the alkaline-earth metal family, which includes strontium (Sr), barium (Ba), magnesium (Mg), beryllium (Be), and radium (Ra), has two valence electrons-a key requirement for creating our qubits.

Calcium was selected for this study to simplify potential experimental procedures. Unlike beryllium, calcium is non-toxic [26], allowing for safer handling without special precautions. Moreover, the wavelengths of the electronic transitions used in qubit design are accessible with the lasers available in our laboratory, which is not the case for some other alkaline-earth atoms like magnesium [27].

1.3.2 Electronic structure of the calcium ion

The ground electronic configuration of calcium is $[Ar]4s^2$, and has an atomic number Z of 20. As part of alkaline-earth elements, it possesses a closed-shell, which is surrounded by two valence electrons. For a calcium Rydberg atom, one of these electrons is in a Rydberg state while the other remains in the ground state of the ion core, or in a low excited state. These electrons can be referred to as the core electron and the Rydberg electron, respectively denoted in this section by $|n_1\ell_1\rangle$ and $|n_2\ell_2\rangle$.

To a very good extent, the two valence electrons can be approximated as independent. Their wavefunctions can be decoupled, neglecting electron-electron exchange and residual interactions, and reduced to a simple tensor product:

$$|\psi\rangle = |n_1\ell_1\rangle\,|n_2\ell_2\rangle\,. \tag{1.7}$$

As a result of this decoupling, the two electrons are no longer indistinguishable, making it possible to excite one electron without affecting the other [28]. This property is crucial for building our qubits. However, the assumption of non-overlapping wave functions is not entirely accurate. In practice, there exists a residual electrostatic interaction between the electrons, which can lead to autoionization [29]. The

electronic structure of the first electronic levels of the ion Ca^+ is shown in Figure 1.6.

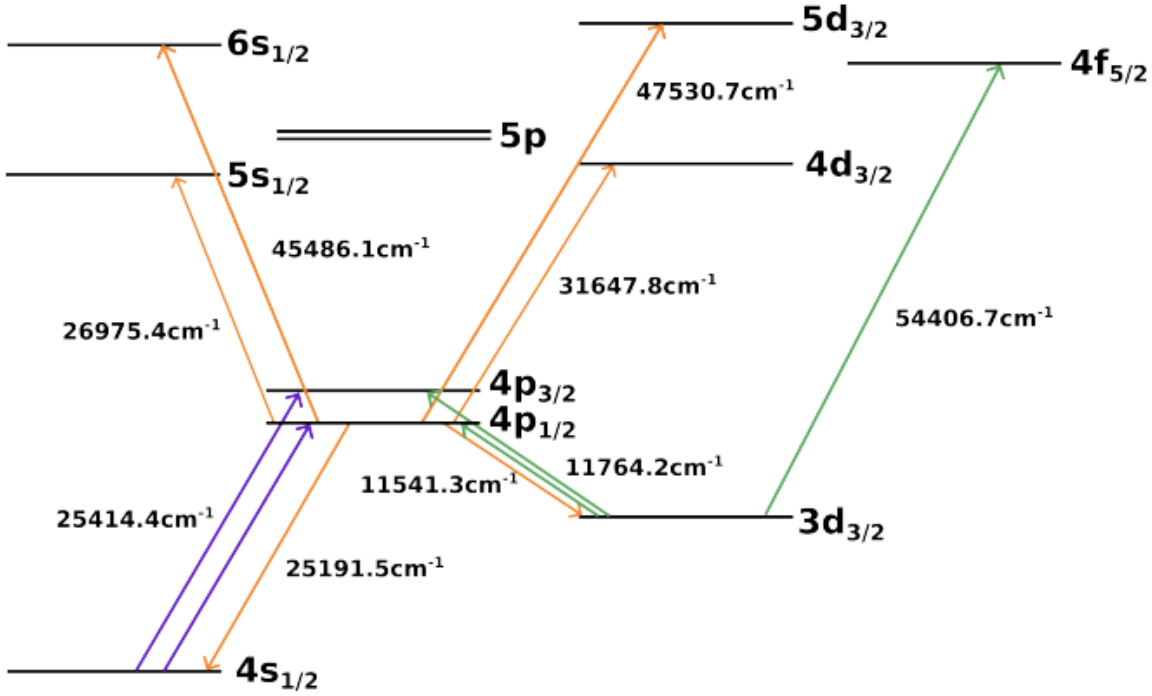

Figure 1.6 – Energy of the first electronic levels of Ca^+, the energy of the different transitions indicated, image from [25].

1.3.3 Valence electrons interaction

jK coupling

To understand the electronic structure of calcium Rydberg atom, it is convenient to start from the structure of the calcium ion Ca^+ and to perturb it by the addition of the Rydberg electron, which perturbs it through the Coulomb interaction between the two electrons. The coupling scheme selected for these two valence electrons is jK coupling, which is commonly used when the outer electron has a sufficiently high orbital angular momentum ($\overrightarrow{\ell_2} > 3$) to limit its core penetration. In this scheme, the total angular momentum of the inner electron ($\overrightarrow{j_1}$) couples with the orbital angular momentum of the outer electron ($\overrightarrow{\ell_2}$) to give the angular momentum $\overrightarrow{K}$ of the two-electron system, excluding the spin $\overrightarrow{s_2}$ of the Rydberg electron. This relationship is expressed as:

$$\overrightarrow{K} = \overrightarrow{\ell_1} + \overrightarrow{s_1} + \overrightarrow{\ell_2}. \tag{1.8}$$

The state vector describing the two valence electrons system in jK coupling can now be written as:

$$|n_1\ell_1 s_1 j_1 n_2\ell_2 K M_K\rangle\,. \tag{1.9}$$

Perturbation theory

The total Hamiltonian of the two-electron system can be expressed as the sum of the Hamiltonians for each individual electron and the interaction between the electrons, represented by the Coulomb interaction $V_{12} = 1/r_{12}$:

$$H = H_1 + H_2 + V_{12}. \tag{1.10}$$

The interaction term V_{12} can be expanded into a multipole series, yielding:

$$H = -\frac{\nabla_1^2}{2} - V(r_1) - \frac{\nabla_2^2}{2} - \frac{1}{r_2} + \sum_{k=1}^{\infty} \frac{r_1^k}{r_2^{k+1}} P_k(\cos\theta_{12}) \tag{1.11}$$

Here, $V(r_1)$ represents the potential energy of the core electron, and $1/r_2$ is the potential energy term for the Rydberg electron due to its Coulomb interaction with the ion. This term has been simplified from its original form $2/r_2$ using the first order of the multipole expansion, indicating that the doubly charged core is screened by the inner electron, resulting in the Rydberg electron interacting with an effective +1 charge. In the valence electron interaction term, we wrote r_1^k/r_2^{k+1} instead of the more general expression $r_<^k/r_>^{k+1}$, with $r_<$ denoting the smallest of the two radii and $r_>$ the largest. This is because the wavefunctions of the core and Rydberg electrons do not significantly overlap and the Rydberg electron is, to a very good approximation, always further than the core electron. $P_k(\cos\theta_{12})$ are Legendre polynomials, where θ_{12} is the angle between $\overrightarrow{r_1}$ and $\overrightarrow{r_2}$, the vectors pointing from the core to the valence electrons.

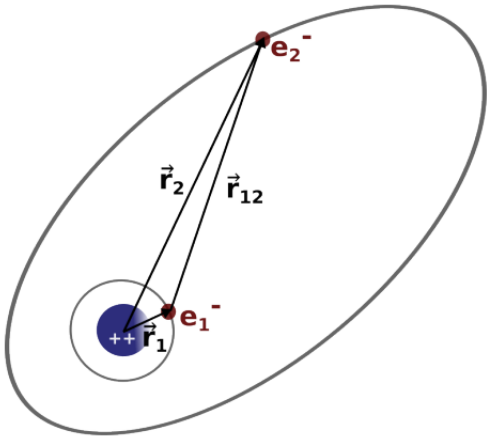

Figure 1.7 – Representation of the calcium Rydberg atom, with the vectors $\overrightarrow{r_1}$ and $\overrightarrow{r_2}$ pointing towards the core and Rydberg electrons, respectively. The Rydberg electron can be considered hydrogen-like due to the screening of the doubly charged core by the inner electron, leading to an effective +1 charge seen by the Rydberg electron.

When the valence electron interaction term is neglected, the total wavefunction of the system reduces to the product of the individual wavefunctions of the Ca^+ ion and the hydrogenic-like wavefunction for the Rydberg electron. Consequently, the total energy is simply the sum of the individual energies.

$$\psi = \psi_{\mathrm{Ca}^+} \otimes \psi_{n_2\ell_2}, \tag{1.12}$$

$$W^{(0)} = W_{\mathrm{Ca}^+(n_1\ell_1)} - \frac{1}{2n_2^2}. \tag{1.13}$$

Energy shift

The energy of the total interacting system can be written in a perturbative expression as:

$$W = W^{(0)} + W^{(1)} + W^{(2)} + \dots. \tag{1.14}$$

Neglecting the exchange interaction between the two valence electrons, the first two order terms are given by [30]:

$$W^{(1)} = \langle n_1\ell_1 s_1 j_1 n_2\ell_2 K M_K | V_{12} | n_1\ell_1 s_1 j_1 n_2\ell_2 K M_K \rangle, \tag{1.15}$$

$$W^{(2)} = \sum_\gamma \frac{|\langle n_1\ell_1 s_1 j_1 n_2\ell_2 K M_K | V_{12} | \gamma \rangle|^2}{W^{(0)}_{n_1\ell_1 s_1 j_1 n_2\ell_2} - W^{(0)}_\gamma}, \tag{1.16}$$

with γ denoting all states other than $|n_1\ell_1 s_1 j_1 n_2\ell_2 K M_K\rangle$. These energy terms cause deviations from the hydrogenic approximation and induce splitting of levels for different K. Following the developments in [25], we derive the following formulas for energy shifts:

- The final expression for the first order energy shift is given by:

$$W^{(1)} \approx -\frac{e}{4\pi\epsilon_0 a_0^3}\frac{4(j_1+1)\Theta(\gamma_1,j_1)f_2}{(2j_1-1)n_2^3\ell_2(\ell_2+1/2)(\ell_2+1)}, \tag{1.17}$$

  where $\Theta(\gamma_1, j_1)$ is the quadrupole moment of the ionic core and f_2 is a geometrical factor.

- The final expression for the second order energy shift is given by:

$$\begin{aligned} W^{(2)}_{n_2\ell_2 K} = \sum_{kn_1'\ell_1'} & \frac{\langle n_1\ell_1|\, r_1^k\, |n_1'\ell_1'\rangle^2}{W_{n_1\ell_1 j_1} - W_{n_1'\ell_1'}} \left\langle \frac{1}{r_2^{2k+2}} \right\rangle_{n_2\ell_2} \\ & \times \Bigg[\sum_{j_1'\ell_2'} C^2_{kKj_1\ell_1\ell_1'\ell_2\ell_2'} + \sum_{j_1'\ell_2'} \frac{\Delta_{n_1'\ell_1'} S_{j_1'} C^2_{kKj_1\ell_1\ell_1'\ell_2\ell_2'}}{W_{n_1\ell_1 j_1} - W_{n_1'\ell_1'}} \\ & + \sum_{j_1'\ell_2'} \frac{\overline{W}_{kn_2\ell_2\ell_2'} C^2_{kKj_1\ell_1\ell_1'\ell_2\ell_2'}}{W_{n_1\ell_1 j_1} - W_{n_1'\ell_1'}} \\ & + 2\sum_{j_1'\ell_2'} \frac{\overline{W}_{kn_2\ell_2\ell_2'} C^2_{kKj_1\ell_1\ell_1'\ell_2\ell_2'} \Delta_{n_1'\ell_1'} S_{j_1'}}{(W_{n_1\ell_1 j_1} - W_{n_1'\ell_1'})^2} \Bigg]. \end{aligned} \tag{1.18}$$

  where W_{nl} is the energy of the corresponding level and $\Delta_{n\ell}$ is the energy difference between the fine-structure components. In this expression, taking only $k = 1$ and $k = 2$ for the dipole and quadrupole contributions, respectively, is sufficiently accurate. The dipole contribution is the main contributor for most levels.

These two equations provide the energy shift of any core level when a high-ℓ_2 Rydberg electron is present. Ultimately, it is necessary to sum these first- and second-order energy shifts over the relevant levels to obtain the energy values of the two-electron system, accounting for the Coulomb interaction between the valence electrons.

Chapter 2

Two qubits architecture

2.1 Description of the project

The objective of this study is to evaluate the feasibility of incorporating two qubits within a single calcium Rydberg atom and to provide foundational guidelines for potential experiments. Traditionally, atoms encoding qubits accommodate one qubit per atom, as demonstrated in calcium-ion trapped systems referenced in [31]. To this end, Chapter 2 will explain the architecture of the proposed system, detailing the design considerations for the selection of electronic levels. Chapter 3 will focus on the implementation of a CNOT gate between the two qubits within the atom. This quantum gate is pivotal in quantum computing, as one of DiVincenzo's criteria for functional qubits is the ability to implement a universal set of gates, a criterion met by the CNOT gate in addition with single-qubit gates (Section 1.1). Possible measurement techniques, as well as single-qubit gates within the atom, will be discussed in Chapter 4.

As explained in Section 1.3, the total wavefunction of the system composed of two valence electrons can be approximated by:

$$|\psi\rangle = |n_2\ell_2\rangle\,|n_1\ell_1\rangle\,, \tag{2.1}$$

where 1 and 2 refer to the core and Rydberg electrons, respectively. The energy of the total interacting system is given by Equation (1.13), with a correction due to the residual Coulomb repulsion between the valence electrons provided in Equation (1.14). We assume that each of these electrons can occupy a pair of levels, denoted as $|n_i\ell_i\rangle \leftrightarrow |n_i'\ell_i'\rangle$, where i represents either the core (1) or Rydberg (2) electron. This effectively forms two two-level systems, or in other words, two qubits. In principle, any two electronic levels of an atom could be used, but aspects such as lifetime and energy differences between them must be considered when

implementing qubits. Previous studies and experiments have shown that ground states and Rydberg levels are suitable for encoding qubits [9].

Outline of our CNOT gate

A two-qubit system is represented in the four-level basis $\{|00\rangle, |01\rangle, |10\rangle, |11\rangle\}$, where the first number represents the state of the first qubit while the second one is for the other qubit. In a non entangled state, the two-qubit system may be written as the tensor product of the two wavefunctions of qubits states,

$$|\psi_{system}\rangle = |\psi_1\rangle \otimes |\psi_2\rangle . \tag{2.2}$$

The CNOT gate prevents a flip of the quantum state of the so-called target qubit (t) under the condition that the so-called control qubit (c) is in state $|0\rangle$. For example, if $|\psi\rangle_c = \alpha |0\rangle_c + \beta |1\rangle_c$ and $|\psi\rangle_t = |0\rangle_t$,

$$|\psi\rangle_c |\psi\rangle_t = \alpha |0\rangle_c |0\rangle_t + \beta |1\rangle_c |0\rangle_t \xrightarrow{\text{CNOT}} \alpha |0\rangle_c |0\rangle_t + \beta |1\rangle_c |1\rangle_t . \tag{2.3}$$

Qubit	Role	$\|\psi_2\rangle \otimes \|\psi_1\rangle$
Rydberg	Control	$\|\psi_2\rangle$
Core	Target	$\|\psi_1\rangle$

Table 2.1 – Role and notation of each qubit.

To realize our CNOT gate, we leverage the energy difference between identical ion-core states interacting with different Rydberg states. Specifically, we exploit the energy difference resulting from Equations (1.17) and (1.18) between the transitions $|10\rangle \leftrightarrow |11\rangle$ and $|00\rangle \leftrightarrow |01\rangle$. By tuning a laser to be resonant with one of these transitions, while it remains off-resonance for the other transition due to the different energy shifts, we can implement the CNOT gate.

When the laser is tuned to be resonant with the $|10\rangle \leftrightarrow |11\rangle$ transition, it induces a state flip of the target qubit only when the control qubit is in state $|1\rangle$. Conversely, if the control qubit is in state $|0\rangle$, the laser is off-resonance for the $|00\rangle \leftrightarrow |01\rangle$ transition, and no state flip occurs. This selective resonance ensures the desired effect of the CNOT gate: flipping the target qubit state conditional on the control qubit state.

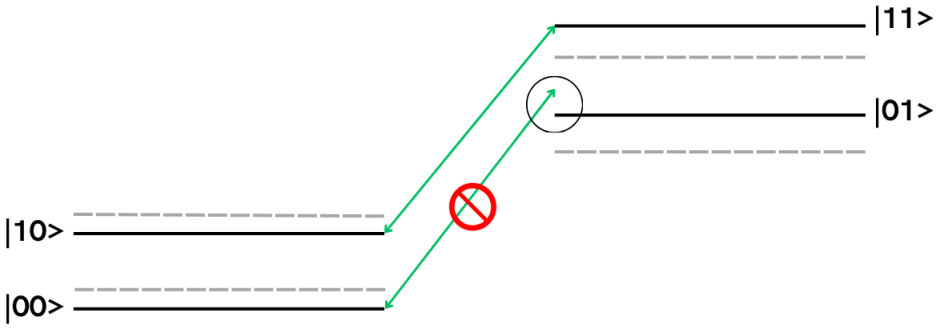

Figure 2.1 – Illustration of our CNOT gate principle: the four levels of the two-qubit system are depicted with black lines (including $W^{(1)} + W^{(2)}$) and gray dotted lines (omitting $W^{(1)} + W^{(2)}$). The laser (green) is resonant with the transition $|10\rangle \leftrightarrow |11\rangle$ but not with the transition $|00\rangle \leftrightarrow |01\rangle$. Not to scale.

The functionality of the CNOT gate relies on the energy difference between these two transitions, as illustrated in Figure 2.1. Therefore, after calculating the energy shifts, the electronic states must be carefully selected to maximize the energy difference between the transitions $|10\rangle \leftrightarrow |11\rangle$ and $|00\rangle \leftrightarrow |01\rangle$.

2.2 Selection of electronic levels

2.2.1 Computation of energy-level shifts

To realize the CNOT gate with high fidelity, the energy difference between the $|00\rangle \leftrightarrow |01\rangle$ and $|10\rangle \leftrightarrow |11\rangle$ transitions must be large. The selected energy levels must satisfy this condition while remaining feasible to prepare experimentally. To identify the most suitable levels, we compute the differential energy-level shifts caused by the residual electronic interaction. For the core levels, the shifts have been calculated for the ion Ca^+ in some of its lowest excited states: the ground state $Ca^+(4s_{1/2})$, $Ca^+(3d_{3/2})$, $Ca^+(4p_{1/2})$, and $Ca^+(5p_{1/2})$. The energy shifts are evaluated when these ion-core states interact with a Rydberg electron whose principal quantum number ranges from $n_2 = 10$ to 60.

In this work, we consider only the first two corrections, $W^{(1)}$ and $W^{(2)}$, as developed in Equations (1.17) and (1.18). Thus, the total energy of the interacting system is:

$$W = W_{Ca^+} - \frac{1}{2n_2^2} + W^{(1)} + W^{(2)}. \tag{2.4}$$

To obtain the second-order energy shift $W^{(2)}$, it is necessary to truncate the sums in Equation (1.18) to a limited number of levels around the concerned one, $(n_1\ell_1)$. The individual contributions to the total energy shift are inversely proportional to the energy separation $W_{n_1\ell_1 j_1} - W_{n_1'\ell_1'}$ between the levels. Therefore, significant contributions to the shift primarily arise from the interaction with nearby states. It is also important to note that the quadrupole contribution ($k = 2$) has been considered only for the $4p_{1/2}$ state, as it is negligible for the other states (see [25], pp. 24-26).
Additionally, to obtain the energy shifts using the formulas from Equations (1.17) and (1.18), certain values were sourced from NIST [27], while others required numerical computation. The method to obtain these computed values is explained below.

1. **Radial dipole integral**

   The radial dipole integrals were calculated using a method described in [25] (pp. 25-26). A summary of the procedure is provided here:

   (a) An angular momentum j_1 is chosen for the initial state (if multiple possibilities exist). The line strength of the transition S (in atomic units) can then be calculated as:

   $$S \equiv \left|\langle n_1 j_1 \|\mathbf{r}_1^{(1)}\| n_1' j_1'\rangle\right|^2 = \frac{(2j_1'+1)A}{2.0261\times 10^{-6}\sigma^3}. \tag{2.5}$$

   Here, A is the Einstein coefficient for spontaneous emission of this transition, given in s^{-1} (sourced from [27]), and σ is the wavenumber of the transition in cm^{-1}. The operator $\mathbf{r}_1^{(1)} = r_1 C^{(1)}$ is an irreducible tensor operator of rank 1, with r_1 representing the radial coordinate of the electron (see [32], p. 307). The double vertical bars $\|$ indicate a reduced matrix element, which can be converted to a matrix element using the Wigner-Eckart theorem.

   (b) The line strength S is used to calculate the reduced matrix element:

   $$\langle n_1\ell_1\|\mathbf{r}_1^{(1)}\|n_1'\ell_1'\rangle = \frac{S^{1/2}(-1)^{\ell_1+j_1'+3/2}}{[j_1,j_1']^{1/2}} \begin{Bmatrix} \ell_1 & s_1 & j_1 \\ j_1' & 1 & \ell_1' \end{Bmatrix}. \tag{2.6}$$

   (c) Finally, the desired matrix element is obtained by separating the angular from the radial part:

$$\langle n_1\ell_1|\, r_1\, |n_1'\ell_1'\rangle = \frac{(-1)^{\ell_1}\langle n_1\ell_1\|\mathbf{r}_1^{(1)}\|n_1'\ell_1'\rangle}{[\ell_1,\ell_1']^{1/2}\begin{pmatrix}\ell_1 & 1 & \ell_1'\\ 0 & 0 & 0\end{pmatrix}}. \tag{2.7}$$

The following table lists the computed values of the matrix elements for the states contributing to the shift of the studied levels.

Matrix element	Transition	Value [a.u.]
$\lvert\langle 4s\rvert\, r_1\, \lvert 4p\rangle\rvert^2$	$4s_{1/2} \leftrightarrow 4p_{1/2}$	13.00
$\lvert\langle 3d\rvert\, r_1\, \lvert 4p\rangle\rvert^2$	$3d_{3/2} \leftrightarrow 4p_{1/2}$	5.10
$\lvert\langle 3d\rvert\, r_1\, \lvert 4f\rangle\rvert^2$	$3d_{3/2} \leftrightarrow 4f_{5/2}$	1.87
$\lvert\langle 4p\rvert\, r_1\, \lvert 4s\rangle\rvert^2$	$4p_{1/2} \leftrightarrow 4s_{1/2}$	13.00
$\lvert\langle 4p\rvert\, r_1\, \lvert 5s\rangle\rvert^2$	$4p_{1/2} \leftrightarrow 5s_{1/2}$	6.64
$\lvert\langle 4p\rvert\, r_1\, \lvert 6s\rangle\rvert^2$	$4p_{1/2} \leftrightarrow 6s_{1/2}$	0.49
$\lvert\langle 4p\rvert\, r_1\, \lvert 3d\rangle\rvert^2$	$4p_{1/2} \leftrightarrow 3d_{3/2}$	5.10
$\lvert\langle 4p\rvert\, r_1\, \lvert 4d\rangle\rvert^2$	$4p_{1/2} \leftrightarrow 4d_{3/2}$	14.48
$\lvert\langle 4p\rvert\, r_1\, \lvert 5d\rangle\rvert^2$	$4p_{1/2} \leftrightarrow 5d_{3/2}$	1.13
$\lvert\langle 4p\rvert\, r_1^2\, \lvert 4p\rangle\rvert^2$	$4p_{1/2} \leftrightarrow 4p_{3/2}$	472.19*
$\lvert\langle 5p\rvert\, r_1\, \lvert 5s\rangle\rvert^2$	$5p_{1/2} \leftrightarrow 5s_{1/2}$	58.16
$\lvert\langle 5p\rvert\, r_1\, \lvert 6s\rangle\rvert^2$	$5p_{1/2} \leftrightarrow 6s_{1/2}$	26.95
$\lvert\langle 5p\rvert\, r_1\, \lvert 7s\rangle\rvert^2$	$5p_{1/2} \leftrightarrow 7s_{1/2}$	1.71
$\lvert\langle 5p\rvert\, r_1\, \lvert 3d\rangle\rvert^2$	$5p_{1/2} \leftrightarrow 3d_{3/2}$	0.03
$\lvert\langle 5p\rvert\, r_1\, \lvert 4d\rangle\rvert^2$	$5p_{1/2} \leftrightarrow 4d_{3/2}$	41.64
$\lvert\langle 5p\rvert\, r_1\, \lvert 5d\rangle\rvert^2$	$5p_{1/2} \leftrightarrow 5d_{3/2}$	41.70
$\lvert\langle 5p\rvert\, r_1\, \lvert 6d\rangle\rvert^2$	$5p_{1/2} \leftrightarrow 6d_{3/2}$	3.71
$\lvert\langle 5p\rvert\, r_1^2\, \lvert 5p\rangle\rvert^2$	$5p_{1/2} \leftrightarrow 5p_{1/2}$	8445.81*

Table 2.2 – Values of radial integrals for the states in the vicinity of the studied ion-core states. Tables are for ion-core states $Ca^+(4s_{1/2})$, $Ca^+(3d_{3/2})$, $Ca^+(4p_{1/2})$, and $Ca^+(5p_{1/2})$. The matrix elements $\lvert\langle 4p\rvert\, r_1^2\, \lvert 4p\rangle\rvert^2$ and $\lvert\langle 5p\rvert\, r_1^2\, \lvert 5p\rangle\rvert^2$ (quadrupole moment) were calculated numerically (private communication: M. Génévriez).

2. **Energy differences**

The energy differences $W_{n_1\ell_1 j_1} - W_{n_1'\ell_1'}$ are computed by considering the respective weights of each spin-orbit multiplet (p. 27, [25]). For example, the energy difference between $W_{4p_{1/2}} - W_{3d}$ is calculated as follows:

$$W_{4p_{1/2}} - W_{3d} = 25191.51 - \left(13650.19 + \frac{3}{5}\cdot 60.7\right) = 11504.9\,\mathrm{cm}^{-1}. \tag{2.8}$$

The factor 3/5 arises from the statistical weight between the multiplicities of the $3d_{3/2}$ and $3d_{5/2}$ states.

Energy difference	Value [a.u.]
$W_{4s_{1/2}} - W_{4p}$	-0.115
$W_{3d_{3/2}} - W_{4p}$	-0.053
$W_{3d_{3/2}} - W_{4f}$	-0.248
$W_{4p_{1/2}} - W_{4s}$	0.115
$W_{4p_{1/2}} - W_{5s}$	-0.123
$W_{4p_{1/2}} - W_{6s}$	-0.207
$W_{4p_{1/2}} - W_{3d}$	0.052
$W_{4p_{1/2}} - W_{4d}$	-0.144
$W_{4p_{1/2}} - W_{5d}$	-0.217
$W_{4p_{1/2}} - W_{4p}$	-0.0007
$W_{5p_{1/2}} - W_{5s}$	0.038
$W_{5p_{1/2}} - W_{6s}$	-0.046
$W_{5p_{1/2}} - W_{7s}$	-0.086
$W_{5p_{1/2}} - W_{3d}$	0.213
$W_{5p_{1/2}} - W_{4d}$	0.068
$W_{5p_{1/2}} - W_{5d}$	-0.056
$W_{5p_{1/2}} - W_{6d}$	-0.091
$W_{5p_{1/2}} - W_{5p}$	-0.0002

Table 2.3 – Energy differences accounting for the weights of spin-orbit multiplets of states in the vicinity of the studied ion-core states used to calculate the second-order energy shift $W^{(2)}$.

3. **Spin-orbit splittings**

The fine-structure splittings, denoted as $\Delta_{n_1'\ell_1'}$, are calculated using the energy differences between fine-structure components. The previously determined energy differences are refined using $S_{j_1'}$, which is given by the following expression:

$$S_{j_1'} = \frac{j_1'(j_1'+1) - \ell_1'(\ell_1'+1) - 3/4}{2\ell_1' + 1}. \tag{2.9}$$

And the fine-structure splitting is:

$$\Delta_{n_1'\ell_1'} = \frac{W_{n_1\ell_1 j_1} - W_{n_1'\ell_1'}}{S_{j_1'}}. \tag{2.10}$$

Quantity	Value [a.u.]
Δ_{3d}	3.46×10^{-5}
Δ_{4d}	1.09×10^{-5}
Δ_{5d}	5.0×10^{-6}
Δ_{6d}	2.64×10^{-6}
Δ_{4p}	1.02×10^{-3}
Δ_{5p}	3.67×10^{-4}
Δ_{4f}	0

Table 2.4 – Spin-orbit splittings of states in the vicinity of the studied ion-core states used in the calculations to obtain the second-order energy shift $W^{(2)}$. Levels with $\ell_1 = 0$ (s-states) do not appear as they do not exhibit fine structure.

At the end of the analysis, we can numerically compute both the first and second-order energy shifts for each combination of studied ion-core states, namely $Ca^+(4s_{1/2})$, $Ca^+(3d_{3/2})$, $Ca^+(4p_{1/2})$, $Ca^+(5p_{1/2})$, paired with Rydberg states having principal quantum numbers ranging from $n_2 = 10$ to 60.
As for n_2, the choice of the orbital quantum number of the Rydberg electron, ℓ_2, is also crucial, as the energy shifts are also dependent on this parameter. The penetration of the Rydberg electron in the ion-core region, which varies with ℓ_2, affects the second-order energy shift $W^{(2)}$ through terms such as $\left\langle \frac{1}{r_2^{2k+2}} \right\rangle_{n_2\ell_2}$. Additionally, ℓ_2 plays a direct role in the formula for the first-order energy shift at the denominator, as given in Equation (1.17).
To determine the appropriate quantum numbers for each level basis states of the two qubits $|0\rangle_c, |1\rangle_c, |0\rangle_t$ and $|1\rangle_t$, we have plotted graphs of the total energy shift $W^{(1)} + W^{(2)}$ in Figure 2.2(a) and 2.2(b). These plots display four curves corresponding to different ion-core levels, with a fixed n_2 and varying ℓ_2 on the x-axis, as well as the reverse scenario for varying n_2 and fixed ℓ_2.

It is also important to mention that due to the jK coupling between the two valence electrons presented in Equation (1.8), the total system will split into different K-levels, each exhibiting distinct energy shifts. The ion-core states $[Ca^+(4s_{1/2})n_2\ell_2]_K$, $[Ca^+(4p_{1/2})n_2\ell_2]_K$, and $[Ca^+(5p_{1/2})n_2\ell_2]_K$, where the ion-core has a total orbital momentum of $j_1 = 1/2$, will split into two different K-levels:

$$j_1 = 1/2 \Rightarrow \ell_2 - \frac{1}{2} < K < \ell_2 + \frac{1}{2}, \tag{2.11}$$

while the $[Ca^+(3d_{3/2})n_2\ell_2]_K$ levels will split into four different K-levels:

$$j_1 = 3/2 \Rightarrow \ell_2 - \frac{3}{2} < K < \ell_2 + \frac{3}{2}. \tag{2.12}$$

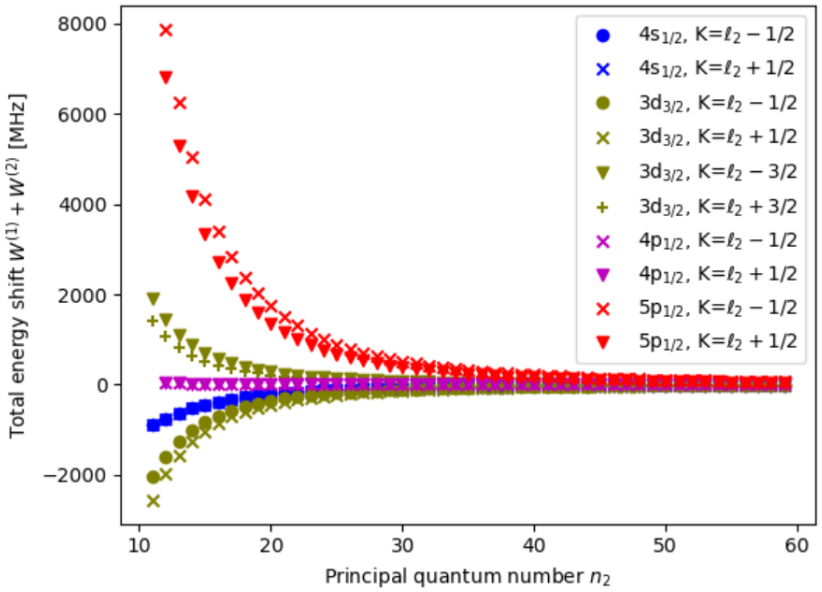

((a)) Variation of the total energy shift $W^{(1)} + W^{(2)}$ with respect to n_2 for $\ell_2 = 11$.

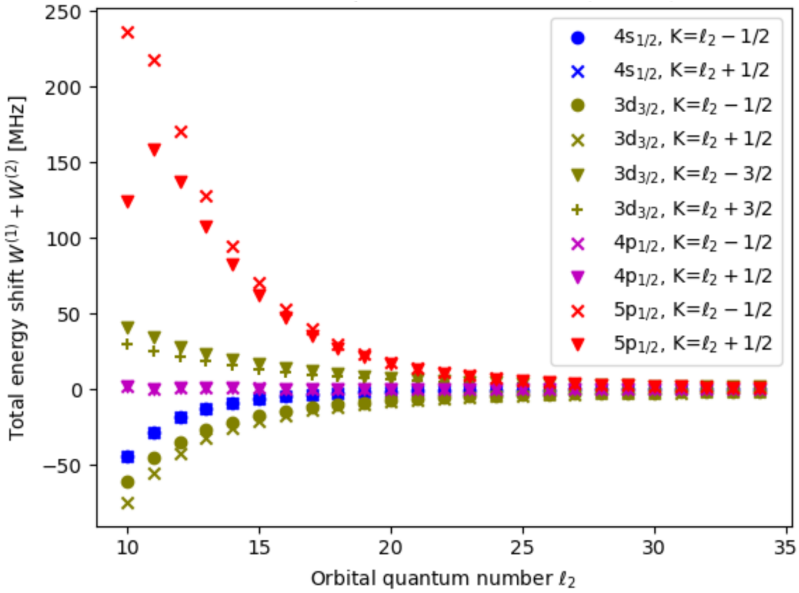

((b)) Variation of the total energy shift $W^{(1)} + W^{(2)}$ with respect to ℓ_2 for $n_2 = 40$.

Figure 2.2 – Variations of the total energy shift $W^{(1)} + W^{(2)}$ for different parameters. (a) With respect to n_2 for $\ell_2 = 11$. (b) With respect to ℓ_2 for $n_2 = 40$. In both cases, different colored curves are for different ion-core states (n_1, ℓ_1) studied.

2.2.2 Discussion of the results and determination of levels

The first noticeable observation from Figure 2.2(a) and 2.2(b) is that, regardless of the ion-core state, the total energy shift increases when n_2 or ℓ_2 decreases. This behavior is expected when n_2 is reduced: physically, decreasing n_2, therefore the distance, between the electrons results in an increased Coulomb interaction leading to a larger energy shift.
Regarding the increase in the total energy shift with decreasing ℓ_2, an explanation can be found by examining the first order energy shift in Equation (1.17). Here, ℓ_2 appears in the denominator, indicating that $W^{(1)} \propto \ell_2^{-3}$.
Now, let us determine the levels for the two qubits.

1. **Ion-core qubit**

   Aside from the significant energy shift between the transitions $|00\rangle \leftrightarrow |01\rangle$ and $|10\rangle \leftrightarrow |11\rangle$, which is essential for implementing our CNOT gate, another critical factor impacting the quality of our qubits is the lifetime of these states. The qubit states must be protected against decoherence to achieve higher fidelity. Consequently, the calcium ion ground state $Ca^+(4s_{1/2})$, with an effectively infinite lifetime, is a clear choice for $|0\rangle_c$.

   When selecting $|1\rangle_c$, despite the large energy shift associated with the $Ca^+(5p_{1/2})$ state, its relatively short lifetime of approximately 40 ns [33] makes it unsuitable. In contrast, the metastable state $Ca^+(3d_{3/2})$, with a much longer lifetime of 1.2 s [34], is a more viable candidate. A similar reasoning applies to the $Ca^+(4p_{1/2})$ state, which has a very short lifetime of around 6 ns [33], making it less favorable compared to the $Ca^+(5p_{1/2})$ state, and even less so compared to the $Ca^+(3d_{3/2})$.

2. **Rydberg qubit**

   When selecting the levels for the Rydberg qubit, in addition to considering the magnitude of the energy shift, the lifetime of the levels should also be considered. The radiative lifetime of the Rydberg states scales as n^3 for low ℓ, and as n^5 for circular states (see Section 1.2.1). We have decided to select $n_2 = 40$ and $n_2 = 42$ for $|0\rangle_t$ and $|1\rangle_t$, respectively. The typical lifetime for these quantum numbers, dominated by black-body radiation [18], is around 100 µs, which seems acceptable. The exact lifetime will be calculated in Section 3.3.3. For the orbital quantum number ℓ_2 of the Rydberg qubit, selecting low values would lead to high autoionization rates [35]. Moreover, the model used to calculate the energy shifts, summarized in this thesis and developed in detail in [25], requires corrections for low ℓ_2 values due to the non-adapted coupling scheme (Section 1.3.3). Therefore, we have chosen

$\ell_2 = 11$ and $\ell_2 = 13$ for $|0\rangle_t$ and $|1\rangle_t$, respectively.

Selecting orbital quantum numbers with a difference $\Delta\ell_2 = 2$ between the two basis states of the Rydberg qubit allows us to achieve a larger difference in energy shifts for implementing the CNOT gate than by keeping the same ℓ_2 for both states. The relatively small difference of $\Delta_{\ell_2} = 2$ also maintains feasible transitions within a single qubit using two photons. Then, interactions between Rydberg states are generally strongest for similar orbital quantum numbers, and therefore it is common to have small $\Delta\ell$ for Rydberg-Rydberg qubits [9].

Qubit state	$\|0\rangle$	$\|1\rangle$
Rydberg qubit	$\|40, 11\rangle$	$\|42, 13\rangle$
Core qubit	$\left\|\mathrm{Ca}^+(4s_{1/2})\right\rangle$	$\left\|\mathrm{Ca}^+(3d_{3/2})\right\rangle$

Table 2.5 – Levels of each qubit, the Rydberg qubit denoted as $|n_2\ell_2\rangle$.

In this work, we do not consider a specific K-splitting as representing a single qubit state. Instead, the two-level states involving $\mathrm{Ca}^+(4\mathrm{s}_{1/2})$, namely $|00\rangle$ and $|10\rangle$, are treated as the average of their two K-splittings, $\ell_2 - 1/2$ and $\ell_2 + 1/2$. For the two-level states involving $\mathrm{Ca}^+(3\mathrm{d}_{3/2})$, namely $|01\rangle$ and $|11\rangle$, we only consider the two (out of four) K-splittings with a positive energy shift $\ell_2 - 3/2$ and $\ell_2 + 3/2$ (Figure 2.2(b) and 2.2(a)).

This approximation is reasonably valid because the K-level pairs mentioned are nearly degenerate; the energy differences between them are minimal and, therefore, do not significantly affect the efficacy of the CNOT gate. The specific K-level occupied by the electron does not influence the CNOT gate mechanism as long as the transition can occur.
However, in practice, the selection rules for jK coupling must be derived to determine which K-levels are accessible during transitions. Once this is established, it is essential to verify whether a single laser is sufficient to drive transitions between different K-levels.
By examining the energy differences between K-level pairs from another study [25], which considered states with similar quantum numbers, it becomes evident that selecting a laser with a sufficiently broad linewidth would enable driving all relevant transitions.

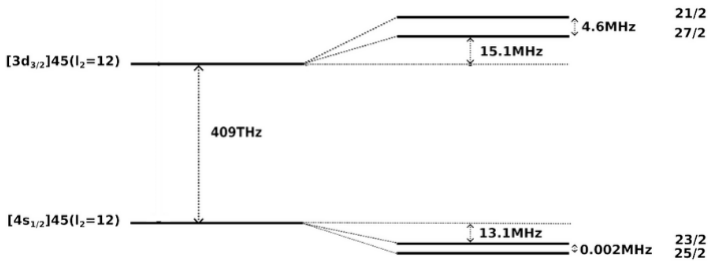

Figure 2.3 – Representation of the splitting between K-levels from [25]. The K-level pairs depicted are $[\mathrm{Ca}^+(3d_{3/2})45,12]_{K=12\pm3/2}$ and $[\mathrm{Ca}^+(4s_{1/2})45,12]_{K=12\pm1/2}$.

The two K-levels of the $[\mathrm{Ca}^+(4s_{1/2})n_2\ell_2]_{K=\ell_2\pm1/2}$ state are separated by only $\approx$ 2kHz and are, therefore, hardly distinguishable. In contrast, for the K-level pair of $[\mathrm{Ca}^+(3d_{3/2})n_2\ell_2]_{K=\ell_2\pm3/2}$ state, the splitting is larger, $\approx$ 4.6MHz. The selection rule for transitions in jK coupling is $\Delta K = 0, \pm1$, meaning that both upper levels ($K = 21/2$ and $27/2$) can be reached from either lower level ($K = 23/2$ and $25/2$). Moreover, since the splitting of the upper levels is large compared to the typical laser linewidth used in quantum information experiments, they can be easily distinguished. This is more challenging for the lower levels, whose splitting is comparable to, or smaller than, typical laser linewidths. In this case, they can be considered degenerate. These considerations justify our approximation of the full system as a two-level system.

By selecting the K-splittings that point in opposite directions, specifically by choosing the K-level pair $[\mathrm{Ca}^+(3d_{3/2})n_2\ell_2]_{K=\ell_2\pm3/2}$ instead of $[\mathrm{Ca}^+(3d_{3/2})n_2\ell_2]_{K=\ell_2\pm1/2}$, we can achieve a greater energy difference between the transitions $|00\rangle \leftrightarrow |01\rangle$ and $|10\rangle \leftrightarrow |11\rangle$. Specifically, when the Rydberg qubit is in the $|1\rangle$ state, the splitting is smaller for the states $[\mathrm{Ca}^+(4s_{1/2})n_2\ell_2]_{K=\ell_2\pm1/2}$, where it is negative (relative to the non-shifted energy levels), and larger for the states $[\mathrm{Ca}^+(3d_{3/2})n_2\ell_2]_{K=\ell_2\pm3/2}$, where it is positive (relative to the non-shifted energy levels). This choice results in a larger energy difference between the transitions $|10\rangle \leftrightarrow |11\rangle$ and $|00\rangle \leftrightarrow |01\rangle$.

To simplify notation in this work, when referring to these specific levels, we will use $\mathrm{Ca}^+(4\mathrm{s}_{1/2})n_2\ell_2$ and $\mathrm{Ca}^+(3\mathrm{d}_{3/2})n_2\ell_2$, rather than the more detailed expressions $[\mathrm{Ca}^+(4\mathrm{s}_{1/2})n_2\ell_2]_{K=\ell_2\pm1/2}$ and $[\mathrm{Ca}^+(3\mathrm{d}_{3/2})n_2\ell_2]_{K=\ell_2\pm3/2}$, respectively.

Atomic configuration	Two-qubit state	$W^{(1)} + W^{(2)}$ [MHz]
$Ca^+(4s_{1/2})40, 11$	$\|00\rangle$	-28.24
$Ca^+(3d_{3/2})40, 11$	$\|01\rangle$	29.75
$Ca^+(4s_{1/2})42, 13$	$\|10\rangle$	-10.86
$Ca^+(3d_{3/2})42, 13$	$\|11\rangle$	17.92

Table 2.6 – Total energy shift for the four states of the two-qubit system.

Figure 2.4 – Representation of the two-qubit system with the corresponding energy differences: the energy shift with respect to the levels omitting $W^{(1)} + W^{(2)}$ (gray arrows), the laser detuning (red arrow), the CNOT laser frequency (green arrows) and levels transition (black arrows).

In the end, the total energy difference achieved between the two transitions of the CNOT gate is therefore $(W_{00}^{(1)+(2)} - W_{01}^{(1)+(2)}) - (W_{10}^{(1)+(2)} - W_{11}^{(1)+(2)})$, which gives 29.21 MHz. This value ensures the blockade of the transition $|00\rangle \leftrightarrow |01\rangle$ when a laser is resonant with the transition $|10\rangle \leftrightarrow |11\rangle$.

Chapter 3

CNOT gate simulation

The aim of this section is to numerically simulate the effect of our CNOT gate on a quantum system composed of two qubits within a single calcium atom, as explained in Chapter 2. To achieve this, the quantum system is described by an effective Hamiltonian, with its interaction with the laser realizing the CNOT gate modeled semi-classically through an additional interaction term in the Hamiltonian. The incoherent time evolution of the system is accounted for using the Lindblad master equation, which allows us to study the system's decoherence and evaluate the CNOT gate's performances, such as gate fidelity and operation time. All simulations are conducted in Python using the `QuTiP` library [36]. The first part of this section focuses on determining the interaction between a laser and an atom under different approximations, which are essential for constructing the Hamiltonian used in the simulations.

3.1 Quantum system description

3.1.1 Light-matter interaction

An atom interacts with a monochromatic electromagnetic field characterized by frequency ω, wave vector $\mathbf{k}$, and vector potential $\mathbf{A}$. The equations in this section are presented for an atom with a single electron, but they can be generalized to multiple electrons by summing over the nabla operator in Equation (3.1) and over the position vectors of different electrons in Equation (3.2). The Hamiltonian is given by [37]:

$$H = H_0 - \frac{i}{\hbar}\mathbf{A} \cdot \nabla = H_0 + H_I, \tag{3.1}$$

where H_0 represents the Hamiltonian of the atom, and H_I is the interaction Hamiltonian, which depends on time due to the vector potential $\mathbf{A}(\mathbf{r}, t)$, with $\mathbf{r}$

denoting the position vector of the electron.

$$\mathbf{A}(\mathbf{r},t) = A_0(\omega)\boldsymbol{\epsilon}e^{i(\mathbf{k}\cdot\mathbf{r}-\omega t+\delta_\omega)} + \text{c.c.}. \tag{3.2}$$

Here, $A_0(\omega)$ represents the amplitude of the electromagnetic wave, and $\boldsymbol{\epsilon}$ denotes the polarization vector.
To solve this Hamiltonian, we use the Schrödinger equation:

$$i\hbar\frac{\partial}{\partial t}\Psi(\mathbf{r},t) = H(t)\Psi(\mathbf{r},t). \tag{3.3}$$

The perturbation caused by the electromagnetic field is typically weak compared to the Coulomb attraction of the atomic core, and thus only weakly perturbs the electronic levels. Perturbation theory allows us to compute an approximate solution to Equation (3.3). Considering a two-level system with energies E_1 and E_2 for the respective levels, and a normalized wavefunction $|\Psi(t)\rangle$, we can write:

$$|\Psi(t)\rangle = c_1(t)\,|1\rangle\, e^{-i\frac{E_1 t}{\hbar}} + c_2(t)\,|2\rangle\, e^{-i\frac{E_2 t}{\hbar}}. \tag{3.4}$$

Substituting the wavefunction from Equation (3.4) into the Schrödinger equation, we obtain the following for the coefficients $c_1(t)$ and $c_2(t)$, after defining $(E_1 - E_2)/\hbar = \omega_{12}$:

$$\begin{aligned}\dot{c}_1(t) = -A_0(\omega)\Big[&\Big\langle 1\Big|\boldsymbol{\epsilon}e^{i\mathbf{k}\cdot\mathbf{r}}\cdot\nabla\Big|2\Big\rangle\, c_2(t)e^{i(\omega_{12}-\omega)t}e^{i\delta_\omega}\\ &+\Big\langle 1\Big|\boldsymbol{\epsilon}e^{-i\mathbf{k}\cdot\mathbf{r}}\cdot\nabla\Big|2\Big\rangle\, c_2(t)e^{i(\omega_{12}+\omega)t}e^{-i\delta_\omega}\Big],\end{aligned} \tag{3.5}$$

$$\begin{aligned}\dot{c}_2(t) = -A_0(\omega)\Big[&\Big\langle 2\Big|\boldsymbol{\epsilon}e^{i\mathbf{k}\cdot\mathbf{r}}\cdot\nabla\Big|1\Big\rangle\, c_1(t)e^{i(\omega_{12}-\omega)t}e^{i\delta_\omega}\\ &+\Big\langle 2\Big|\boldsymbol{\epsilon}e^{-i\mathbf{k}\cdot\mathbf{r}}\cdot\nabla\Big|1\Big\rangle\, c_1(t)e^{i(\omega_{12}+\omega)t}e^{-i\delta_\omega}\Big].\end{aligned} \tag{3.6}$$

Assuming the system is initially in state $|1\rangle$, i.e., $c_1(0) = 1$, and that, since the perturbation caused by the electromagnetic field is weak, $c_1(t) \approx 1$ at all times, we can write the following integrals:

$$\begin{aligned}c_2(t) = -A_0(\omega)\Big[&\Big\langle 2\Big|\boldsymbol{\epsilon}e^{i\mathbf{k}\cdot\mathbf{r}}\cdot\nabla\Big|1\Big\rangle\, e^{i\delta_\omega}\int_0^t e^{i(\omega_{12}-\omega)T}dT\\ &+\Big\langle 2\Big|\boldsymbol{\epsilon}e^{-i\mathbf{k}\cdot\mathbf{r}}\cdot\nabla\Big|1\Big\rangle\, e^{-i\delta_\omega}\int_0^t e^{i(\omega_{12}+\omega)T}dT\Big].\end{aligned} \tag{3.7}$$

When the electromagnetic wave is near resonance with the transition frequency ω_{12}, the term $e^{i(\omega_{12}+\omega)}$ oscillates very rapidly and can be averaged to zero over any

reasonable interaction time. This is known as the rotating-wave approximation (RWA). Neglecting the second integral, we have:

$$c_2(t) = -A_0(\omega) \left\langle 2 \left| \boldsymbol{\epsilon} e^{i\mathbf{k}\cdot\mathbf{r}} \cdot \nabla \right| 1 \right\rangle e^{i\delta_\omega} \int_0^t e^{i(\omega_{12}-\omega)T} dT. \tag{3.8}$$

We define the transition moment $M_{21}(\omega) = \left\langle 2 \left| \boldsymbol{\epsilon} e^{i\mathbf{k}\cdot\mathbf{r}} \cdot \nabla \right| 1 \right\rangle$. The population evolution can then be found as:

$$|c_2(t)|^2 = A_0^2(\omega)|M_{21}(\omega)|^2 \left| e^{i\delta_\omega} \int_0^t e^{i(\omega_{12}-\omega)T} dT \right|^2. \tag{3.9}$$

The right side of this equation is evaluated in [37] (p. 112-114) and gives, for sufficiently long times, $2\pi t$. Let us assume that the electromagnetic field is monochromatic, so we can write $A_0(\omega_{21})$ and $M_{21}(\omega_{21})$. Knowing that the intensity of an electromagnetic field with frequency ω is [37] (p. 114):

$$I(\omega) = 2\epsilon_0 \omega^2 c A_0^2(\omega), \tag{3.10}$$

it yields

$$|c_2(t)|^2 = \frac{4\pi^2}{c} \frac{I(\omega_{21})}{\omega_{21}^2} |M_{21}(\omega_{21})|^2 t = W_{21} t. \tag{3.11}$$

The value W_{21} is the absorption rate, indicating that the probability for the atom to be in state $|2\rangle$ increases linearly with time at a rate W_{21}.

Dipole approximation

Consider the matrix element $M_{21}(\omega_{21}) = \left\langle 2 \left| \boldsymbol{\epsilon} e^{i\mathbf{k}\cdot\mathbf{r}} \cdot \nabla \right| 1 \right\rangle$. The exponential term $e^{i\mathbf{k}\cdot\mathbf{r}}$ can be expanded as:

$$e^{i\mathbf{k}\cdot\mathbf{r}} = 1 + i\mathbf{k}\cdot\mathbf{r} + \frac{1}{2!}(i\mathbf{k}\cdot\mathbf{r})^2 + \dots. \tag{3.12}$$

Given that the characteristic size of the atom is large compared to $|\mathbf{k}|$ (where $\mathbf{k}$ has a norm $|\mathbf{k}| = 2\pi/\lambda$), we can approximate $e^{i\mathbf{k}\cdot\mathbf{r}} \approx 1$. Consequently, M_{21} can be rewritten to highlight the dipole moment:

$$M_{21}(\omega_{21}) = -\omega_{21} \left\langle 2 \left| \boldsymbol{\epsilon} \cdot \mathbf{r} \right| 1 \right\rangle. \tag{3.13}$$

Applying the rotating-wave approximation (RWA) to Equation (3.6) and substituting the matrix element with the form given in Equation (3.13), we obtain:

$$\dot{c}_2(t) = A_0(\omega_{21})\omega_{21} \left\langle 2 \left| \boldsymbol{\epsilon} \cdot \mathbf{r} \right| 1 \right\rangle e^{i(\omega_{21}-\omega)t} e^{i\delta_\omega} c_1(t). \tag{3.14}$$

Using Equation (3.10) to replace $A_0(\omega_{21})$ and noting that [37]:

$$I = \frac{1}{2}\epsilon_0 c\mathbf{E}^2, \tag{3.15}$$

we derive:

$$\dot{c}_2(t) = \frac{|\mathbf{E}|}{2} \langle 2 | \boldsymbol{\epsilon} \cdot \mathbf{r} | 1 \rangle e^{i(\omega_{21}-\omega)t} e^{i\delta_\omega} c_1(t). \tag{3.16}$$

Quadrupole approximation

Beyond the first term of the dipolar approximation $e^{i\mathbf{k}\cdot\mathbf{r}} \approx 1$, higher-order terms contribute but more weakly. These terms give rise to weak transitions that are often referred to as "forbidden transitions" [37] p139. The matrix element M_{21}, including the second term $i\mathbf{k}\cdot\mathbf{r}$ and assuming a monochromatic electromagnetic field, can be expressed as [37] p139:

$$M_{21}(\omega_{21}) = -\frac{\omega_{21}}{2c} \langle 2 | \mathbf{l_y} | 1 \rangle - \frac{i\omega_{21}^2}{2c} \langle 2 | (\boldsymbol{\epsilon} \cdot \mathbf{r})(\mathbf{k} \cdot \mathbf{r}) | 1 \rangle , \tag{3.17}$$

where $\mathbf{l_y}$ is the projection of the orbital momentum on the y-axis.
The first term corresponds to the magnetic dipolar transition (M1), while the second term corresponds to the electric quadrupole transition (E2). Substituting the quadrupolar term of M_{21} in Equation (3.6), after the usage of RWA to neglect the second term we have:

$$\dot{c}_2(t) = A_0(\omega_{21}) \left(\frac{-i\omega_{21}^2}{2c} \langle 2 | (\boldsymbol{\epsilon} \cdot \mathbf{r})(\mathbf{k} \cdot \mathbf{r}) | 1 \rangle \right) e^{i(\omega_{21}-\omega)t} e^{i\delta_\omega} c_1(t). \tag{3.18}$$

Using Equation (3.10) for $A_0(\omega)$, we derive:

$$\dot{c}_2(t) = \frac{1}{\omega_{21}} \sqrt{\frac{I}{2\epsilon_0 c}} \left(\frac{-i\omega_{21}^2}{2c} \langle 2 | (\boldsymbol{\epsilon} \cdot \mathbf{r})(\mathbf{k} \cdot \mathbf{r}) | 1 \rangle \right) e^{i(\omega_{21}-\omega)t} e^{i\delta_\omega} c_1(t). \tag{3.19}$$

Substituting Equation (3.15) for I, we obtain:

$$\dot{c}_2(t) = \frac{1}{\omega_{21}} \sqrt{\frac{\frac{1}{2}\epsilon_0 c\mathbf{E}^2}{2\epsilon_0 c}} \left(\frac{-i\omega_{21}^2}{2c} \langle 2 | (\boldsymbol{\epsilon} \cdot \mathbf{r})(\mathbf{k} \cdot \mathbf{r}) | 1 \rangle \right) e^{i(\omega_{21}-\omega)t} e^{i\delta_\omega} c_1(t), \tag{3.20}$$

which simplifies further to:

$$\dot{c}_2(t) = \frac{-i\omega_{21}|\mathbf{E}|}{4c} \langle 2 | (\boldsymbol{\epsilon} \cdot \mathbf{r})(\mathbf{k} \cdot \mathbf{r}) | 1 \rangle e^{i(\omega_{21}-\omega)t} e^{i\delta_\omega} c_1(t). \tag{3.21}$$

3.1.2 Hamiltonian construction

In the previous section, we discussed the coupling between an electromagnetic wave and a quantum system to quantify the strength of the interaction.
Due to our CNOT setup, the Hamiltonian describing the system exhibits off-diagonal coupling between the two-qubit states $|00\rangle$, $|01\rangle$ and $|10\rangle$, $|11\rangle$. This implies that the Hamiltonian elements $\langle 00|\,\hat{H}\,|01\rangle$ and $\langle 10|\,\hat{H}\,|11\rangle$ are non-zero, indicating laser-induced transitions between these states. Similarly, their complex conjugates, $\langle 01|\,\hat{H}\,|00\rangle$ and $\langle 11|\,\hat{H}\,|10\rangle$, are also non-zero.
The couplings between $|00\rangle$ and $|11\rangle$, as well as between $|01\rangle$ and $|10\rangle$, are very small and can be neglected. These correspond to transitions involving changes in the states of both qubits, which are enabled by electron-electron correlations. Since these correlations are particularly weak in our system, a fact we leverage to construct the two qubits, the associated transitions are vanishingly small.
The Hamiltonian for the system can be expressed as, in the $\{|00\rangle, |01\rangle, |10\rangle, |11\rangle\}$ basis:

$$\hat{H} = \begin{bmatrix} 0 & \frac{\Omega}{2} & 0 & 0 \\ \frac{\Omega}{2} & (E_{|01\rangle} - E_{|00\rangle}) - \omega_{laser} & 0 & 0 \\ 0 & 0 & (E_{|10\rangle} - E_{|00\rangle}) & \frac{\Omega}{2} \\ 0 & 0 & \frac{\Omega}{2} & (E_{|11\rangle} - E_{|00\rangle}) - \omega_{laser} \end{bmatrix}. \tag{3.22}$$

The different terms composing this Hamiltonian will be evaluated in this section.

Figure 3.1 – Representation of the two-qubit system with the corresponding energy differences: the energy shift with respect to the levels omitting $W^{(1)} + W^{(2)}$ (gray arrows), the laser detuning (red arrow), the laser frequency (green arrows) and levels transition (black arrows).

Diagonal terms

The quantities $E_{|00\rangle}, E_{|01\rangle}, E_{|10\rangle}, E_{|11\rangle}$ represent the energy levels of the corresponding states. In the Hamiltonian, the matrix element $\langle 00| \hat{H} |00\rangle$ has been set to zero to simplify the calculations. Consequently, $E_{|00\rangle}$ has been subtracted from the other diagonal elements. This corresponds to changing the phase of the wavefunction by an overall phase factor, which is allowed in quantum mechanics since the wavefunction is defined up to an arbitrary phase.
The total energy of each basis state can be determined using the following equation from Section 2.4:

$$W = W_{\mathrm{Ca}^+(n_1\ell_1)} - \frac{1}{2n_2^2} + W^{(1)} + W^{(2)}, \tag{3.23}$$

where the values for $W^{(1)}+W^{(2)}$ are taken from Table 2.6, and $W_{\mathrm{Ca}^+(n_1\ell_1)}$ is sourced from [27].

The final step for the diagonal elements is to include the interaction with the laser in these terms. When the laser is resonant with the transition $|10\rangle \leftrightarrow |11\rangle$, the photon energy ω_{laser} perfectly matches the energy difference between $E_{|11\rangle}$ and $E_{|10\rangle}$, i.e., $\omega_{\text{laser}} = E_{|11\rangle} - E_{|10\rangle}$. Thus, the Hamiltonian becomes:

$$\hat{H} = \begin{bmatrix} 0 & \frac{\Omega}{2} & 0 & 0 \\ \frac{\Omega}{2} & (E_{|01\rangle} - E_{|00\rangle}) - \omega_{\text{laser}} & 0 & 0 \\ 0 & 0 & (E_{|10\rangle} - E_{|00\rangle}) & \frac{\Omega}{2} \\ 0 & 0 & \frac{\Omega}{2} & (E_{|11\rangle} - E_{|00\rangle}) \end{bmatrix}, \tag{3.24}$$

with the values completing it provided in Table 3.1.

Quantity	Energy [a.u.]	Energy [MHz]
$E_{\|00\rangle} - E_{\|00\rangle}$	0	0
$E_{\|01\rangle} - E_{\|00\rangle}$	0.06219	409 221 049
$E_{\|10\rangle} - E_{\|00\rangle}$	2.9056×10^{-5}	191 178
$E_{\|11\rangle} - E_{\|00\rangle}$	0.06222	409 412 198
ω_{laser}	0.06219	409 221 020
$E_{\|01\rangle} - E_{\|00\rangle} - \omega_{\text{laser}}$	4.4395×10^{-9}	29

Table 3.1 – Total energies of each basis state of the two-qubit system relative to the basis state $|00\rangle$, energy of the laser photon and the value of the diagonal element $\langle 01| \hat{H} |01\rangle$ of the Hamiltonian corresponding to the system.

Off-diagonal terms

The off-diagonal terms in the Hamiltonian represent the coupling between different basis states. For an electric dipole transition (E1), as developed in Equation (3.16), we have:

$$\dot{c}_2(t) = \frac{\Omega}{2} e^{i(\omega_{21}-\omega)t} e^{i\delta_\omega} c_1(t), \tag{3.25}$$

where the Rabi frequency is given by:

$$\Omega = |\mathbf{E}| \langle 2 | \boldsymbol{\epsilon} \cdot \mathbf{r} | 1 \rangle e^{i\delta_\omega}. \tag{3.26}$$

For electric quadrupole transitions (E2), similar to the case of an electric dipole transition, based on Equation (3.21), we have:

$$\dot{c}_2(t) = \frac{\Omega}{2} e^{i(\omega_{21}-\omega)t} e^{i\delta_\omega} c_1(t), \tag{3.27}$$

where the Rabi frequency is given by:

$$\Omega = \frac{-i\omega_{21}|\mathbf{E}|}{2c} \langle 2 | (\boldsymbol{\epsilon} \cdot \mathbf{r})(\mathbf{k} \cdot \mathbf{r}) | 1 \rangle e^{i\delta_\omega}. \tag{3.28}$$

In our two-qubit setup, the transitions coupled with the laser are $|00\rangle \leftrightarrow |01\rangle$ and $|10\rangle \leftrightarrow |11\rangle$, corresponding to a flip in the state of the core qubit $\mathrm{Ca}^+(4\mathrm{s}_{1/2})$ $\leftrightarrow$ $\mathrm{Ca}^+(3\mathrm{d}_{3/2})$. These transitions, with $\Delta\ell = 2$, are electric quadrupole transitions (E2).

The magnitude of the electric field amplitude vector $\mathbf{E}$ is calculated using Equation (3.15). For our calculations, we consider typical laser parameters that can be achieved in the laboratory. We assume the laser has the usual Gaussian spatial profile (TEM00 mode), a waist $w_0 = 1$ mm, and a power of 1 W:

$$|\mathbf{E}| = \sqrt{\frac{2P}{\pi\epsilon_0 c w_0^2}}. \tag{3.29}$$

The value of the quadrupole matrix element $\langle 2 | (\boldsymbol{\epsilon} \cdot \mathbf{r})(\mathbf{k} \cdot \mathbf{r}) | 1 \rangle$ has been computed in [38] to be 8.691 a.u.
Given these parameters, the Rabi frequency for the quadrupole transition is found to be 5.939×10^{-11} a.u., or 0.391 MHz.

3.2 Light dressing

To identify the optimal two-qubit architecture, another setup was investigated in this work. The idea is to couple a laser near resonance with the ion-core state $Ca^+(3d_{3/2})$ and another ion-core state. This approach could potentially enhance the performance of the CNOT gate and improve qubit operation. One key factor that could be optimized is the gate speed, which is related to the magnitude of the Rabi frequency of the transitions $|00\rangle \leftrightarrow |01\rangle$ and $|10\rangle \leftrightarrow |11\rangle$. Specifically, the gate speed directly depends on the Rabi frequency of the ion-core qubit transition $|0\rangle \leftrightarrow |1\rangle$, while the Rydberg qubit state remains unchanged.

Without dressing, the Rabi frequency of the ion-core transition $|0\rangle \leftrightarrow |1\rangle$ is relatively low (0.391 MHz) due to the quadrupole transition between the states $Ca^+(4s_{1/2})n_2\ell_2$ and $Ca^+(3d_{3/2})n_2\ell_2$ ($\Delta\ell_1 = 2$), in contrast to a dipole transition such as that between $Ca^+(4s_{1/2})n_2\ell_2$ and $Ca^+(4p_{1/2})n_2\ell_2$.

When a laser is near resonance with a transition, it creates "dressed states" [39], which are coherent superpositions of the two states connected by the nearly resonant laser. The coefficients describing this superposition depend on the laser's proximity to resonance. If the $|01\rangle$ and $|11\rangle$ states now correspond to $Ca^+(3d_{3/2})n_2\ell_2$ states with some $Ca^+(4p_{1/2})n_2\ell_2$ character admixed by laser dressing, we can expect an increase in the Rabi frequency of the $|00\rangle \leftrightarrow |01\rangle$ and $|10\rangle \leftrightarrow |11\rangle$ transitions. Indeed, the $Ca^+(4s_{1/2})n_2\ell_2 \leftrightarrow Ca^+(4p_{1/2})n_2\ell_2$ transition is an E1 transition with a significantly larger Rabi frequency.

However, alongside the enhancement of the Rabi frequency, there are some drawbacks. The short lifetime of the $4p_{1/2}$ state significantly reduces the lifetime of the dressed state compared to the $3d_{3/2}$ state alone, thus introducing decoherence. These effects will be examined in this section to determine the viability of such a mixture of states.

A laser that is off-resonant with the transition $3d_{3/2} \leftrightarrow 4p_{1/2}$ interacts with these states. This interaction can be represented by the Hamiltonian of the two-level system in the basis $\{Ca^+(3d_{3/2})n_2\ell_2, Ca^+(4p_{1/2})n_2\ell_2\}$, with a distinct Hamiltonian for each of the two Rydberg states:

$$\hat{H} = \begin{bmatrix} E_{Ca^+(3d_{3/2})40,11} & \Omega/2 \\ \Omega/2 & E_{Ca^+(4p_{1/2})40,11} - \omega_{\text{laser}}, \end{bmatrix}, \tag{3.30}$$

and

$$\hat{H} = \begin{bmatrix} E_{Ca^+(3d_{3/2})42,13} & \Omega/2 \\ \Omega/2 & E_{Ca^+(4p_{1/2})42,13} - \omega_{\text{laser}} \end{bmatrix}, \tag{3.31}$$

where $\Omega = \Omega_{3d-4p}$ is the Rabi frequency of the dipole transition $3d_{3/2} \leftrightarrow 4p_{1/2}$. The detuning between the laser for the dressing and the transition is:

$$\delta_{n_2,\ell_2} = E_{\mathrm{Ca}^+(4p_{1/2})n_2\ell_2} - E_{\mathrm{Ca}^+(3d_{3/2})n_2\ell_2} - \omega_{\mathrm{laser}}. \tag{3.32}$$

This detuning, δ_{n_2,ℓ_2}, varies with the state of the Rydberg electron because the energy difference between the states $\mathrm{Ca}^+(4p_{1/2})n_2\ell_2$ and $\mathrm{Ca}^+(3d_{3/2})n_2\ell_2$ differs for each $(n_2\ell_2)$ combination, while the same laser is used in both situations. The detuning must account for these small variations.

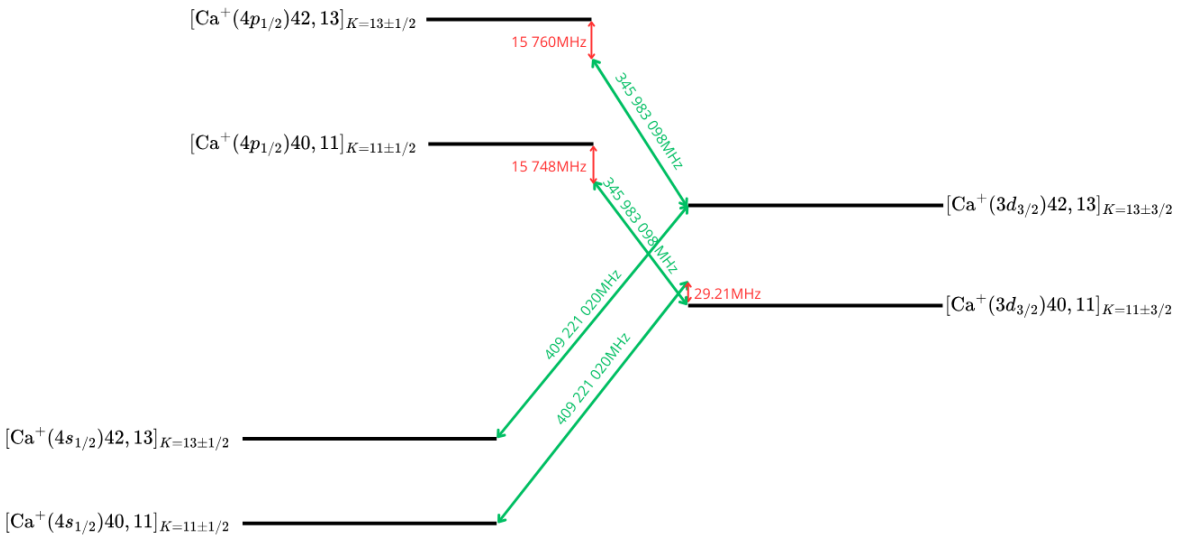

Figure 3.2 – Dressing of states $\mathrm{Ca}^+(3\mathrm{d}_{3/2})n_2\ell_2$ with $\mathrm{Ca}^+(4\mathrm{p}_{1/2})n_2\ell_2$: electronic levels are depicted with black lines (including $W^{(1)} + W^{(2)}$), and lasers with green arrows. The laser used for state dressing is detuned from resonance (red arrow) with the transition between $\mathrm{Ca}^+(3\mathrm{d}_{3/2})n_2\ell_2$ and $\mathrm{Ca}^+(4\mathrm{p}_{1/2})n_2\ell_2$.

To determine the coefficients $\alpha_{n_2\ell_2}$ and $\beta_{n_2\ell_2}$ that describe the superposition of the states $\mathrm{Ca}^+(3d_{3/2})n_2\ell_2$ and $\mathrm{Ca}^+(4p_{1/2})n_2\ell_2$, the Hamiltonians in Equations (3.30) and (3.31) must be diagonalized. This process yields the following expressions:

$$\left|\psi^+_{n_2\ell_2}\right\rangle = \alpha^+_{n_2\ell_2}\left|\mathrm{Ca}^+(3d_{3/2})n_2\ell_2\right\rangle + \beta^+_{n_2\ell_2}\left|\mathrm{Ca}^+(4p_{1/2})n_2\ell_2\right\rangle, \tag{3.33}$$

$$\left|\psi^-_{n_2\ell_2}\right\rangle = \alpha^-_{n_2\ell_2}\left|\mathrm{Ca}^+(3d_{3/2})n_2\ell_2\right\rangle + \beta^-_{n_2\ell_2}\left|\mathrm{Ca}^+(4p_{1/2})n_2\ell_2\right\rangle. \tag{3.34}$$

Analytically, these coefficients can be found using [40]:

$$\left|\psi^+_{n_2\ell_2}\right\rangle = \cos\theta\left|\mathrm{Ca}^+(3d_{3/2})n_2\ell_2\right\rangle + \sin\theta\left|\mathrm{Ca}^+(4p_{1/2})n_2\ell_2\right\rangle, \tag{3.35}$$

$$\left|\psi^-_{n_2\ell_2}\right\rangle = -\sin\theta\left|\mathrm{Ca}^+(3d_{3/2})n_2\ell_2\right\rangle + \cos\theta\left|\mathrm{Ca}^+(4p_{1/2})n_2\ell_2\right\rangle, \tag{3.36}$$

resulting in $\alpha^+_{n_2\ell_2} = \beta^-_{n_2\ell_2}$ and $\alpha^+_{n_2\ell_2} = -\beta^-_{n_2\ell_2}$. The angle θ is given by:

$$\tan 2\theta = \Omega/(E_{\mathrm{Ca}^+(3d_{3/2})n_2\ell_2} - E_{\mathrm{Ca}^+(4p_{1/2})n_2\ell_2}), \tag{3.37}$$

where Ω is the Rabi frequency of the transition between the dressed states.

The purpose of this dressing is to replace the initial basis states $|01\rangle$ and $|11\rangle$ of the two-qubit system in the Hamiltonian describing the CNOT gate (Equation (3.24)) with new states $\psi^+_{n_2\ell_2}$ (or $\psi^-_{n_2\ell_2}$), which are superpositions of the initial state $\mathrm{Ca}^+(3d_{3/2})n_2\ell_2$ and the state $\mathrm{Ca}^+(4p_{1/2})n_2\ell_2$. In this work, the selected eigenstate, primarily composed of the $\mathrm{Ca}^+(3d_{3/2})n_2\ell_2$ state to avoid large decoherence, will be denoted as $\psi^+_{n_2\ell_2}$. Conversely, the $\psi^-_{n_2\ell_2}$ eigenstate is mainly composed of the $\mathrm{Ca}^+(4p_{1/2})n_2\ell_2$ state.

To form the Hamiltonian in Equations (3.30) and (3.31), we need the Rabi frequency of the $3d_{3/2} \leftrightarrow 4p_{1/2}$ transition for the off-diagonal terms.
The Rabi frequency is computed from the radial dipole integral, which can be obtained as explained in Section 2.2.1. This radial integral is then converted to the transition dipole matrix element using Wigner symbols, as detailed in [32], pp. 410-412:

$$\begin{aligned}\langle n\ell|\,\mathbf{r}^{(1)}_1\,|n'\ell'\rangle = \sqrt{[\ell,\ell']}\sqrt{[j,j']}&\begin{pmatrix} \ell' & 1 & \ell \\ 0 & 0 & 0 \end{pmatrix} \\ &\begin{Bmatrix} \ell' & 1/2 & j' \\ j & 1 & \ell \end{Bmatrix} \\ &\begin{pmatrix} j' & 1 & j \\ -m_{j'} & q & m_j \end{pmatrix} \langle n\ell|\,r_1\,|n'\ell'\rangle\,.\end{aligned} \tag{3.38}$$

The polarization state chosen for this calculation is $q = 0$, and the quantum number m_j is selected as 0.5 for both the $4p_{1/2}$ and $3d_{3/2}$ states. The expression $[\ell,\ell']$ equals $(2\ell+1)(2\ell'+1)$, and we have neglected the sign in this equation, as it does not affect our situation.
The laser parameters are identical to those used in the CNOT gate in Equation (3.29). We notice that this Rabi frequency (≈ 210MHz) is logically almost 1000 times higher than that of the quadrupole transition $4s_{1/2} \leftrightarrow 3d_{3/2}$ (≈ 0.391MHz).

Quantity	Value [a.u.]
Radial dipole integral $\left\langle 3d_{3/2}\right\vert r_1 \left\vert 4p_{1/2}\right\rangle$	2.25
Transition matrix element $\left\langle 3d_{3/2}\right\vert \mathbf{r}_1^{(1)} \left\vert 4p_{1/2}\right\rangle$	1.07
Rabi frequency $\Omega_{3d\leftrightarrow 4p}$	3.193×10^{-8}

Table 3.2 – Values of quantities used to calculate the Rabi frequency for the $3d_{3/2} \leftrightarrow 4p_{1/2}$ transition, and the Rabi frequency itself.

The detuning between the laser and the transition must be carefully chosen: if the laser is resonant, it will induce full population transfer from the $3d_{3/2}$ state, thereby significantly reducing the lifetime of the $\psi^+_{n_2\ell_2}$ state due to the short lifetime of the $4p_{1/2}$ state.
After several simulation trials, the photon energy of the laser utilized for the dressing was set to:

$$\omega_{\text{laser}} = E_{\text{Ca}^+(4p_{1/2})42,13} - E_{\text{Ca}^+(3d_{3/2})42,13} - 10\Omega_{3d-4p}, \tag{3.39}$$

which equals 345,983,098 MHz.
This photon energy corresponds to a large detuning from the transition energy, aimed at achieving a slight mixing with the $4p_{1/2}$ state to minimize significant decoherence. The specific values of this dressing are shown in Table 3.3.

Quantity	$\vert 01\rangle = \psi^+_{40,11}$	$\vert 11\rangle = \psi^+_{42,13}$
Detuning $\delta_{n_2\ell_2}$ [MHz]	15,748	15,760
Proportion of $\left\vert 3d_{3/2}\right\rangle$	99.752%	99.876%

Table 3.3 – Characteristics of the dressing of state $3d_{3/2}$ with state $4p_{1/2}$.

In the end, with the new two-qubit states $|01\rangle$ and $|11\rangle$ given by $\psi^+_{n_2\ell_2}$, the Rabi frequency included in the Hamiltonian describing the CNOT gate in Equation (3.24) changes and can be computed as follows:

$$\Omega_{|00\rangle\leftrightarrow|01\rangle} = (\alpha^+_{40,11})^2\Omega_{4s-3d} + (\beta^+_{40,11})^2\Omega_{4s-4p}, \tag{3.40}$$

$$\Omega_{|10\rangle\leftrightarrow|11\rangle} = (\alpha^+_{42,13})^2\Omega_{4s-3d} + (\beta^+_{42,13})^2\Omega_{4s-4p}. \tag{3.41}$$

Specifically, $\Omega_{|00\rangle\leftrightarrow|01\rangle}$ and $\Omega_{|10\rangle\leftrightarrow|11\rangle}$ correspond respectively to the Rabi frequencies of the transitions $|00\rangle \leftrightarrow |01\rangle$ and $|10\rangle \leftrightarrow |11\rangle$. Their values are shown in Table 3.4. It is evident that $\Omega_{|00\rangle\leftrightarrow|01\rangle}$ and $\Omega_{|10\rangle\leftrightarrow|11\rangle}$ are nearly three times larger than $\Omega_{4s\leftrightarrow 3d}$, indicating that the time required for the gate operation has been reduced by a factor of three due to the dressing of the ion-core state $3d_{3/2}$.

Rabi Frequency	Value [a.u.]	Value [MHz]
$\Omega_{\|00\rangle\leftrightarrow\|01\rangle}$	1.499×10^{-10}	0.986
$\Omega_{\|10\rangle\leftrightarrow\|11\rangle}$	1.489×10^{-10}	0.980
$\Omega_{4s\leftrightarrow 3d}$	5.939×10^{-11}	0.391
$\Omega_{4s\leftrightarrow 4p}$	3.613×10^{-8}	237.709
$\Omega_{4p\leftrightarrow 3d}$	3.193×10^{-8}	210.107

Table 3.4 – Rabi frequencies with dressed states for transitions $|00\rangle \leftrightarrow |01\rangle$ (first row), $|10\rangle \leftrightarrow |11\rangle$ (second row), and Rabi frequencies without dressed states for transitions $4s \leftrightarrow 3d$ (third row) and $4s \leftrightarrow 4p$ (fourth row), this latter is calculated following the same process as the Rabi frequency for the transition $4p_{1/2} \leftrightarrow 3d_{3/2}$ which has been explained in this section.

3.3 Incoherent relaxation processes

The simulation accounts for incoherent relaxation processes which impact the behavior of the system. Decoherence occurs as a result of these relaxation processes, leading to a loss of information. These processes are listed in this section and have been incorporated into the numerical simulation after calculating their rates and determining how their effects can be implemented.

3.3.1 Autoionization

When the ion-core of a Rydberg divalent atom is excited, it can decay, among other things, through a mechanism called autoionization. In this process, the atom loses an electron, transitioning from a neutral state Z to the ionized state with $Z-1$ electrons. This mechanism occurs when the total energy of the atom is above the first ionization threshold. For Rydberg states with low orbital angular momentum, the autoionization rate is several orders of magnitude faster than the fluorescence decay of either the ion core or the Rydberg electron [41].
Autoionization can happen when different channels with different ion-core states interact, leading to two possible scenarios. In the first scenario, the energy of the atom in the $n_1\ell_1 n_2\ell_2$ state is lower than the first ionization threshold. Thus, interaction with another channel results in an energy shift between these two channels, as indicated by the red arrow in Figure 3.3. In the second scenario, the total energy is higher than an ionization threshold. In this case, autoionization occurs, as shown by the dotted green arrow, and the Rydberg electron goes towards the ionization continuum.

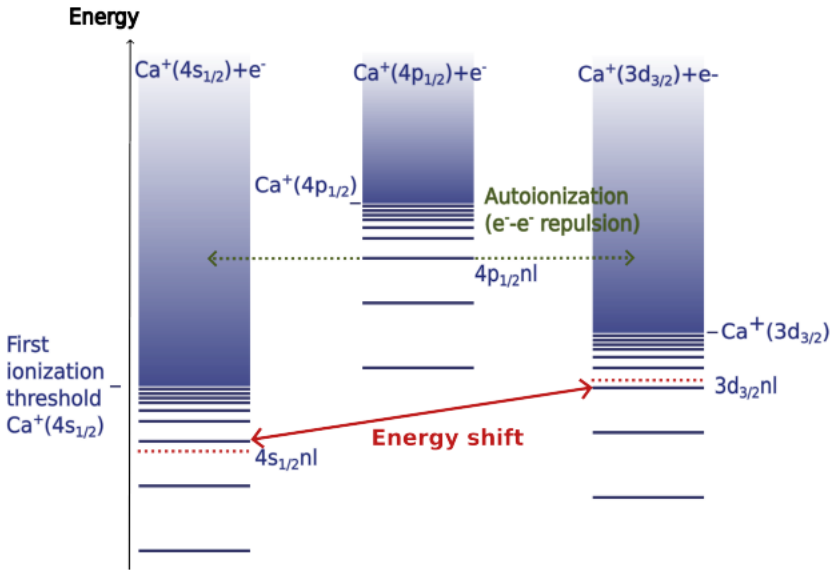

Figure 3.3 – Illustration of the autoionization mechanism for the calcium atom from [25]: autoionization of the $4p_{1/2}nl$ state towards its two neighboring channels, $Ca^+(3d_{3/2})$ and $Ca^+(4s_{1/2})$.

For our two qubits, autoionization can only occur when the ion-core state is $Ca^+(3d_{3/2})$, and not for $Ca^+(4s_{1/2})$, which is the ground state and therefore lower in energy than any other channel.
For the case with the dressed state, the autoionization rate Γ of the state $\psi^+_{n_2\ell_2}$ can be determined as:

$$\Gamma_{\psi^+_{40,11}} = (\alpha^+_{40,11})^2 \Gamma_{Ca^+(3d_{3/2})40,11} + (\beta^+_{40,11})^2 \Gamma_{Ca^+(4p_{1/2})40,11}, \tag{3.42}$$

$$\Gamma_{\psi^+_{42,13}} = (\alpha^+_{42,13})^2 \Gamma_{Ca^+(3d_{3/2})42,13} + (\beta^+_{42,13})^2 \Gamma_{Ca^+(4p_{1/2})42,13}. \tag{3.43}$$

Here, $(\alpha^+_{n_2\ell_2})^2$ and $(\beta^+_{n_2\ell_2})^2$ represent the respective populations of $Ca^+(3d_{3/2})n_2\ell_2$ and $Ca^+(4p_{1/2})n_2\ell_2$ for the dressed state $\psi^+_{n_2\ell_2}$. The autoionization rates, which measure the speed of this phenomenon, are listed in Table 3.5. These values, which depend on the total angular momentum J of the two-electron system, correspond to the highest Γ among the possible J values. This approach is taken to simulate the worst-case scenario.

State	Autoionization rate Γ [a.u.]	Autoionization lifetime τ [s]
$Ca^+(3d_{3/2})40, 11$	2.76×10^{-15}	8.77×10^{-3}
$Ca^+(3d_{3/2})42, 13$	2.45×10^{-15}	9.88×10^{-3}
$Ca^+(4p_{1/2})40, 11$	1.59×10^{-13}	1.52×10^{-4}
$Ca^+(4p_{1/2})42, 13$	3.38×10^{-16}	7.14×10^{-2}
$\psi^+_{40,11}$	3.15×10^{-15}	7.69×10^{-3}
$\psi^+_{42,13}$	2.44×10^{-15}	9.90×10^{-3}

Table 3.5 – Autoionization rates in atomic units and corresponding lifetimes in seconds for the states of interest. Values taken from [29].

3.3.2 Spontaneous emission of ion-core states

Spontaneous emission is the process in which an electron transitions from an excited energy state to a lower energy state, emitting a quantized amount of energy in the form of a photon.
In our situation, spontaneous emission occurs only when the core qubit is in its state $|1\rangle$, corresponding to the $Ca^+(3d_{3/2})$ state or when the core qubit is in the $\psi^+_{n_2\ell_2}$ state for the dressed state scenario. In this latter situation, the spontaneous emission is mainly dominated by the $Ca^+(4p_{1/2})$ state.

The spontaneous emission rate can be computed based on the summation of the Einstein coefficients of the neighboring states of these excited states. These Einstein coefficients,represent the radiative decay rate between two states and therefore it yields:

$$\Gamma_{n_1\ell_1} = \sum_{n_1'\ell_1'} A_{n_1\ell_1 \to n_1'\ell_1'} = \frac{1}{\tau_{n_1\ell_1}}. \tag{3.44}$$

In the scenario with the dressed states, the radiative decay rate of $\psi^+_{n_2 ell_2}$ is determined in the same way as for autoionization, with the coefficients describing the states superposition. In this case, the decay rate of the ion-core states $Ca^+(3d_{3/2})$ or $Ca^+(4p_{1/2})$ does not depend on the state of the Rydberg electron ($\Gamma_{Ca^+(3d_{3/2}40,11} = \Gamma_{Ca^+(3d_{3/2}42,13)}$), because this phenomenon only concerns the ion-core. For the dressed states, the rates are given by:

$$\Gamma_{\psi^+_{n_2\ell_2}} = (\alpha^+_{n_2\ell_2})^2 \Gamma_{Ca^+(3d_{3/2})} + (\beta^+_{n_2\ell_2})^2 \Gamma_{Ca^+(4p_{1/2})}. \tag{3.45}$$

The calculated values are referenced in Table 3.6.

State	Radiative decay rate Γ [a.u.]	Radiative lifetime τ [s]
$Ca^+(3d_{3/2})n_2\ell_2$	2.02×10^{-17}	1.20
$Ca^+(4p_{1/2})n_2\ell_2$	3.64×10^{-9}	6.64×10^{-9}
$\psi^+_{40,11}$	9.05×10^{-12}	2.67×10^{-6}
$\psi^+_{42,13}$	9.04×10^{-12}	2.68×10^{-6}

Table 3.6 – Radiative decay rates in atomic units and corresponding lifetimes in seconds for the states of interest, with values from [34] and [33].

We can see that even with a small proportion of $4p_{1/2}$, less than 0.3% (Table 3.3), the radiative decay rate of the dressed states $\psi^+_{n_2\ell_2}$ is affected by almost 6 orders of magnitude compared to that of $Ca^+(3d_{3/2})$ alone. It is clear that the dressing with the $Ca^+(4p_{1/2})$ state significantly impacts the lifetime.

3.3.3 Rydberg lifetime decay

The decay of Rydberg states is primarily due to two mechanisms: radiative decay (spontaneous emission) and black body radiation-induced transitions to other Rydberg levels [18]. The total lifetime of a Rydberg state can therefore be written as:

$$\frac{1}{\tau^{\mathrm{T}}} = \frac{1}{\tau^{\mathrm{BBR}}} + \frac{1}{\tau^{\mathrm{r}}}. \tag{3.46}$$

Rydberg states are significantly affected by black body radiation because the energy spacing ΔW between these states is small, proportional to $1/n^2$:

$$\Delta W = \frac{1}{2(n'^2 - n^2)}. \tag{3.47}$$

Typically, $\Delta W < kT$ at 300 K [18]. As a result, Rydberg atoms strongly interact with thermal radiation, causing the population initially excited into one Rydberg state to rapidly diffuse to other nearby states. This diffusion is driven by black body radiation-induced dipole transitions.

The black body radiation decay rate is well approximated for large n by [18]:

$$\frac{1}{\tau^{\mathrm{BBR}}} = \frac{4\alpha^3 kT}{3n^2}, \tag{3.48}$$

where α is the fine-strucutre constant. This expression highlights a few interesting points. First, it does not depend on the orbital angular momentum quantum number ℓ. Since the radiative decay rate decreases rapidly with increasing ℓ, for high ℓ states the black body radiation-induced decay rate is often much larger than

the spontaneous emission rate. Second, this trend is further reinforced for high principal quantum numbers n. The black body radiation decay rate $1/\tau^{\mathrm{BBR}}$ varies as $\propto 1/n^2$, while the radiative decay rate varies as $\propto 1/n^3$. Thus, at sufficiently high n and ℓ, the black body radiation-induced decay rate is significantly larger than the spontaneous emission rate.

In our case, with the Rydberg qubit having electronic states with large quantum numbers $n_2 = 40, 42$ and $\ell_2 = 11, 13$, we can assume that the spontaneous emission rate does not significantly affect the total decay rate $1/\tau^T$. The black body radiation-induced decay rate has been computed at room temperature $T = 300$ K for the two Rydberg states, and the values obtained are referenced in Table 3.7.

Rydberg state n_2, ℓ_2	Black body decay rate Γ [a.u.]	Black body lifetime τ [s]
40,11	3.08×10^{-13}	7.85×10^{-5}
42,13	2.79×10^{-13}	8.67×10^{-5}

Table 3.7 – Black body decay rates in atomic units and corresponding lifetimes in seconds for the states of interest.

3.4 Laser pulse simulation

The laser used to implement the CNOT gate is applied to the calcium atom for a duration corresponding to a π-pulse, which fully transfers the population from the state $|10\rangle$ to $|11\rangle$. This pulse duration is determined by the expression:

$$\tau = \frac{\pi}{\Omega_{|10\rangle \leftrightarrow |11\rangle}}, \tag{3.49}$$

where $\Omega_{|10\rangle \leftrightarrow |11\rangle}$ represents the Rabi frequency associated with the transition between $|10\rangle$ and $|11\rangle$. Without dressed states, $\Omega_{|10\rangle \leftrightarrow |11\rangle}$ corresponds to the Rabi frequency of the quadrupole transition $4s_{1/2} \leftrightarrow 3d_{3/2}$. The Rabi frequency for the case with the dressing of the $3d_{3/2}$ state is also provided in Table 3.4. The corresponding pulse durations for both scenarios are presented in Table 3.8.

Core-qubit architecture	Pulse duration [μs]
Without dressing	1.279
With $4p_{1/2}$ dressing	0.510

Table 3.8 – CNOT gate duration for the core qubit state $|1\rangle_c$, without and with dressed states.

To simulate the effect of lasers on the atom, a realistic pulse profile was necessary, incorporating a gradual increase and decrease in power. Given that (see Equation (3.29)):

$$\Omega \propto |\mathbf{E}| \propto \sqrt{P}, \tag{3.50}$$

the Rabi frequency used in the Hamiltonian of Equation (3.24) was modeled to follow the form shown in Figure 3.7. This profile was modeled using a half-period of a sinusoidal function, resulting in a rise time of approximately 50 ns, followed by a constant amplitude until the decrease, which also lasts for 50 ns. This rise and fall time corresponds to 1/10 of the duration of the π-pulse with dressing and 1/30 of the duration without dressing. Using a sinusoidal function followed by a constant value helps to avoid potential discontinuities in the system.

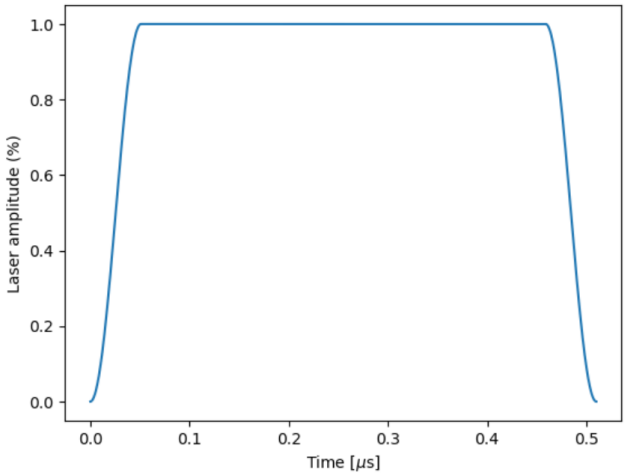

Figure 3.4 – Laser electric field amplitude profile used in the simulation.

3.5 Evolution of the quantum system

To simulate the evolution of a quantum system including incoherent relaxation processes, the Schrödinger equation, which describes the evolution of a quantum state ψ, is not sufficient, as it does not account for incoherent processes such as spontaneous emission, autoionization, or Rydberg lifetime decay.

To accurately simulate the evolution of a quantum system interacting with its environment, the Lindblad master equation is more appropriate. This equation describes the evolution of the density matrix, ρ, which is defined as:

$$\rho = \sum_i p_i \left|\psi_i\right\rangle \left\langle\psi_i\right|, \tag{3.51}$$

where p_i are probabilities and $|\psi_i\rangle$ are the pure states.

The Lindblad master equation governs the time evolution of the density matrix, including incoherent processes. All the approximations made to derive it are detailed in [42], and it is expressed as:

$$\dot{\rho}(t) = -\frac{i}{\hbar}[H(t), \rho(t)] + \sum_n \frac{1}{2}\left(2C_n\rho(t)C_n^\dagger - \rho(t)C_n^\dagger C_n - C_n^\dagger C_n\rho(t)\right), \tag{3.52}$$

where $H(t)$ is the Hamiltonian of the system, and $C_n = \sqrt{\gamma_n}A_n$ are the Lindblad operators that represent different incoherent processes, with their corresponding rates γ_n.

In this work, the evolution of the system after applying the π-pulse required for the CNOT gate has been evaluated using the Lindblad master equation solver provided by the Python library `QuTiP` [36]. `QuTiP` offers a solver through its `mesolve` function. To implement the dissipative processes, a collapse operator has been constructed for each of the processes mentioned in Section 3.3, with the associated rates previously determined. This simulation has been performed multiple times with different initial states. Due to autoionization and the finite Rydberg-state lifetime, a portion of the total initial population is lost, meaning that it no longer occupies any of the qubit states. This proportion of the lost population is also represented in the graphs, labeled as "losses".

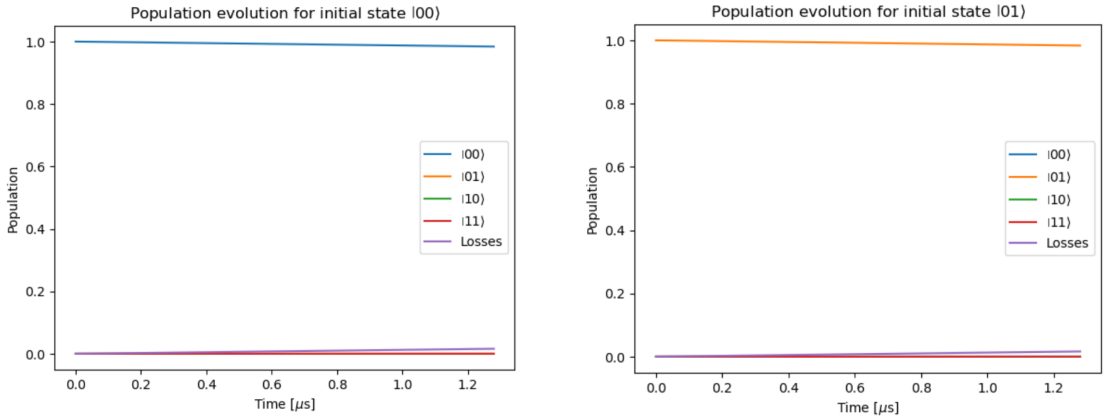

((a))

((b))

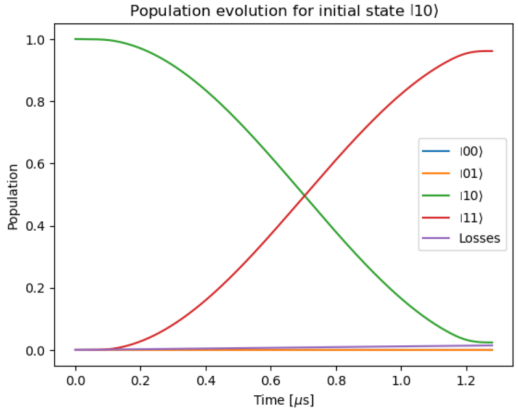

((c))

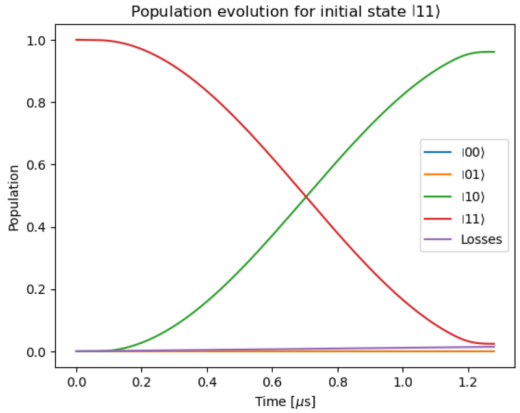

((d))

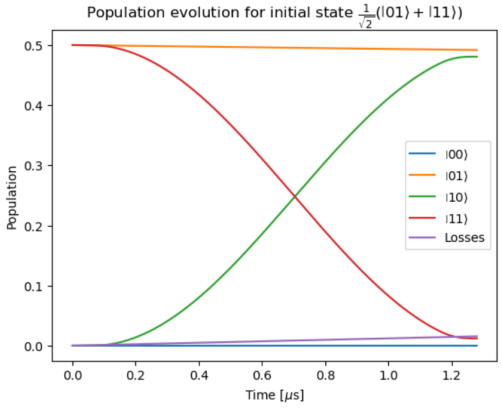

((e))

Figure 3.5 – Population dynamics of the two-qubit system's basis states following the application of the CNOT gate, without state dressing. Each graph corresponds to a different initial state configuration.

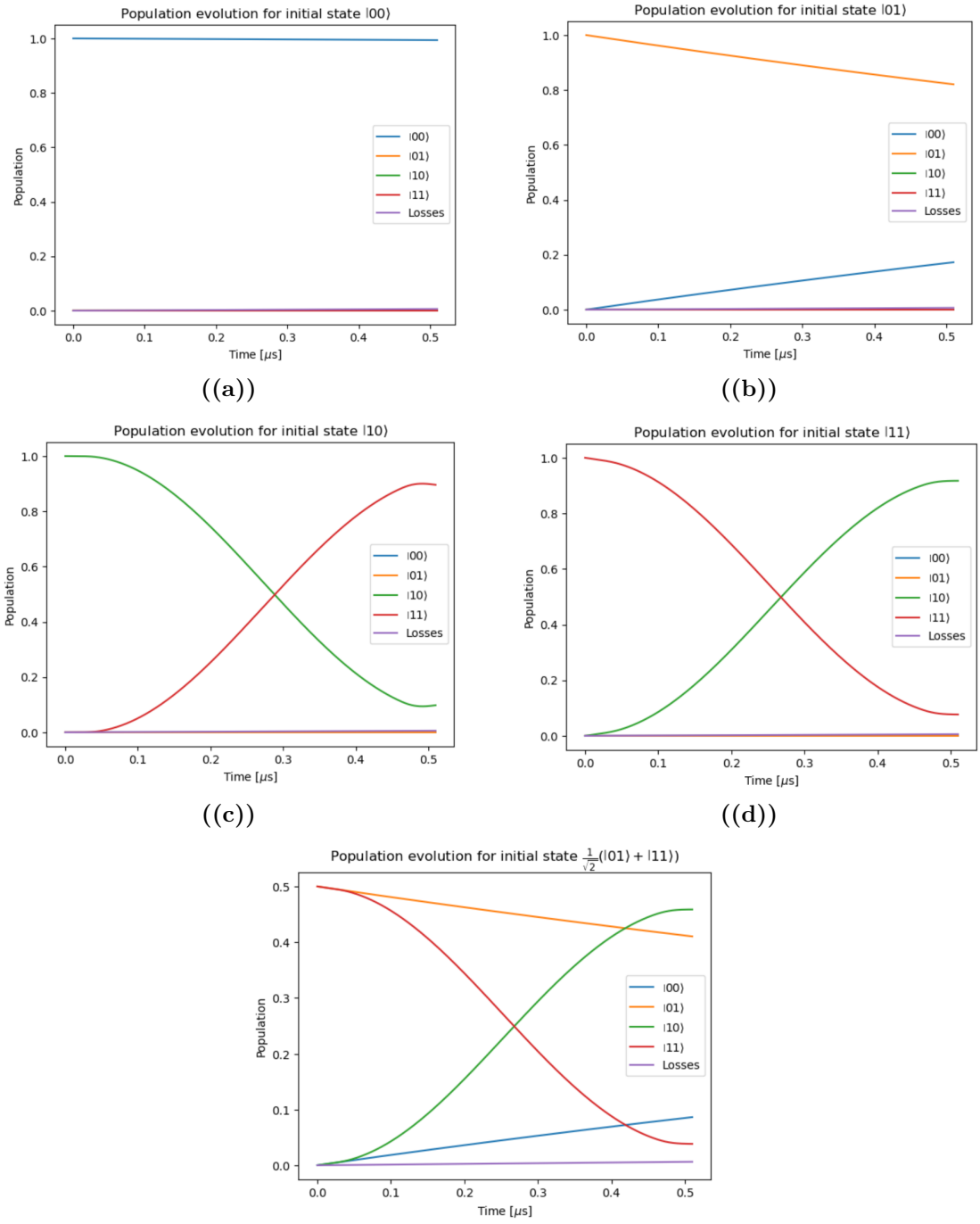

((a)) ((b)) ((c)) ((d)) ((e))

Figure 3.6 – Population dynamics of the two-qubit system's basis states following the application of the CNOT gate, with state dressing of $Ca^+(3d_{3/2})$ with $Ca^+(4p_{1/2})$. Each graph corresponds to a different initial state configuration.

3.6 Results discussion

3.6.1 CNOT performances and fidelity

We can now assess the performance of our CNOT gate, including fidelity, and determine the limiting factors. Additionally, we can compare the two models presented here, with and without dressing of the core qubit.

At first glance, the populations evolve as expected based on the initial state: when the system starts in $|00\rangle$ or $|01\rangle$, the respective populations remain largely constant, while full population transfer occurs when starting in $|10\rangle$ or $|11\rangle$. However, a closer inspection reveals small, rapid oscillations in the populations of the $|00\rangle$ and $|01\rangle$ states whenever either is populated. These oscillations are caused by off-resonant coupling of the $|00\rangle \leftrightarrow |01\rangle$ transition.

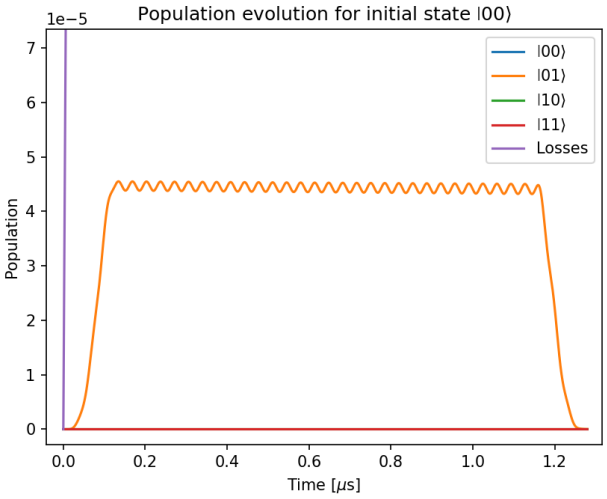

Figure 3.7 – Zoomed-in view of Figure 3.5(a), showing the Rabi oscillations of state $|01\rangle$ while state $|00\rangle$ remains populated. The trapezoidal shape results from the gradual increase in the energy of the laser pulse.

The amplitude and frequency of these oscillations can be found using the following expression for the probability of excitation, as given in [37]:

$$P(t) = \frac{\Omega}{\sqrt{\Omega^2 + \delta^2}} \sin\left(\tilde{\Omega} t\right), \tag{3.53}$$

where $\tilde{\Omega} = \sqrt{\Omega^2 + \delta^2}$ is the generalized Rabi frequency, and δ is the laser detuning relative to the transition.

It is also evident that in the situation with state dressing, the fidelity is more affected: the population in $|11\rangle$ after the application of the CNOT gate on $|10\rangle$ (Figure 3.6(c)) is lower than in the same case without state dressing (Figure 3.5(c)). Incoherent relaxation processes affecting performance are even more visible between Figures 3.6(b) and 3.5(b), where the population in $|01\rangle$ decreases significantly for the first one.

These differences between situations with and without state dressing become more pronounced when the core qubit is in the state $|1\rangle$. Although there is a significant decrease in the population of $|01\rangle$ in Figure 3.5(b), the proportion of losses does not significantly increase, indicating that this cannot be due to autoionization or Rydberg decay, where electrons leave the qubit states. Instead, this must be attributed to spontaneous emission, where electrons decay to the ground state $4s_{1/2}$, thereby flipping the core qubit state. When examining the different lifetimes, the radiative lifetime of $|01\rangle$ is on the order of 10^{-6} s with dressing, but only 1.2 s without it, which confirms our assessment.

Therefore, the primary limiting factor for fidelity in the case of dressed states is the spontaneous emission of the $4p_{1/2}$ state, which significantly impacts the spontaneous emission of the core qubit state $|1\rangle$. While state dressing reduces the gate operation time by a factor of three, it does so at the expense of fidelity. Other relaxation processes, such as autoionization and Rydberg state decay, have lifetimes on the order of 10^{-3} s and 10^{-5} s, respectively.

In the case without state dressing, the limiting factor is the Rydberg state lifetime, which, at nearly 10^{-4} s, is much shorter than the radiative lifetime of the metastable $3d_{3/2}$ state, which is 1.2 s. Lowering the temperature (currently assumed to be room temperature) could enhance the fidelity of this setup. For instance, the Rydberg state lifetime for $n_2 = 42$ at a temperature of 4K (liquid helium temperature) is 6.50×10^{-3} s, compared to 8.67×10^{-5} s at 300K, as shown in [43]. In this scenario, the Rydberg lifetime would become comparable to the autoionization lifetime, making these two factors the new limiting factors for the fidelity which should be enhanced.

Fidelity is a crucial metric for quantifying the similarity between two quantum states. According to the definition provided in [44], p. 409, fidelity between two states represented by their density matrices ρ and σ is given by:

$$F(\rho, \sigma) = \mathrm{tr}\sqrt{\rho^{1/2}\sigma\rho^{1/2}}. \tag{3.54}$$

A more explicit expression is available when calculating fidelity between a pure

state $|\psi\rangle$ and an arbitrary state ρ [44], p. 409:

$$F(|\psi\rangle, \rho) = \sqrt{\langle\psi| \rho |\psi\rangle}. \tag{3.55}$$

In our analysis, we calculate the fidelity between the pure state $|\psi\rangle$, resulting from the application of a theoretically perfect CNOT gate, and the density matrix ρ, obtained after the application of our CNOT gate including all decoherence processes. The computed fidelity values are presented in Table 3.9 below.

Initial state	$\|00\rangle$	$\|01\rangle$	$\|10\rangle$	$\|11\rangle$
Fidelity without dressing	0.9920	0.9917	0.9913	0.9913
Fidelity with dressing	0.9969	0.9054	0.9460	0.9574

Table 3.9 – Fidelities of states after the application of the CNOT gate and their theoretical output.

3.6.2 Entanglement generation and Bell fidelity

A primary interest in using a CNOT gate is its ability to create entanglement, which can be achieved in one additional step. Starting from one of the two-qubit basis states, such as $|01\rangle$, we apply a $\pi/2$ pulse (see Chapter 4), also known as a Hadamard pulse, to the control qubit to create a superposition state. This results in:

$$\frac{1}{\sqrt{2}}(|0\rangle + |1\rangle) \otimes |1\rangle \tag{3.56}$$

The subsequent application of the CNOT gate on this superposition of basis states produces a maximally entangled Bell state, characterized by a wavefunction that cannot be expressed as a product of the individual single-qubit wavefunctions:

$$\frac{1}{\sqrt{2}}(|01\rangle + |11\rangle) \xrightarrow{\text{CNOT}} \frac{1}{\sqrt{2}}(|01\rangle + |10\rangle) = \left|\Psi^+\right\rangle. \tag{3.57}$$

A standard method to characterize the performance of an entangling operation is through the Bell state entanglement fidelity [9], defined as:

$$F_{\text{Bell}} = \left\langle\Psi^+\right| \rho \left|\Psi^+\right\rangle, \tag{3.58}$$

where ρ is the density matrix of the quantum system under evaluation. If the obtained fidelity satisfies $F_{\text{Bell}} > 0.5$, the qubits are considered entangled [9].

In our system, after applying the CNOT gate to perform the operation described in Equation (3.57), the Bell state fidelity achieved was 0.28 with dressed states

and 0.52 without dressing. These values are lower than anticipated, likely due to issues with the coherence of the superposition. Specifically, the diagonal elements of the density matrix after the CNOT gate application closely match the ideal value of 0.5 for the $|01\rangle$ and $|10\rangle$ states. However, the off-diagonal elements, $\langle 01| \rho |10\rangle$ and $\langle 10| \rho |01\rangle$, are significantly lower than the ideal 0.5, suggesting the presence of an incoherent mixture. Enhancing coherence could be achieved by minimizing relaxation processes, such as lowering the temperature to extend the Rydberg state lifetimes.

For comparison, other Bell state fidelities for Rydberg qubits have been reported in the literature. It is important to note that these results correspond to entanglement between two different atoms, whereas our system entangles two electrons within a single atom.
The first demonstration and characterization of a Rydberg quantum gate was conducted in 2010 by the Wisconsin group, where they implemented a CNOT gate between two neutral Rydberg atoms [45]. This experiment achieved entanglement with a Bell state fidelity of $F_{\text{Bell}} = 0.48 \pm 0.06$. After accounting for atom loss, the corrected entanglement fidelity was reported as $F_{\text{Bell}} = 0.58$.
In 2017, the first heteronuclear Rydberg quantum gate was demonstrated [46]. In this work, a CNOT gate based on the Rydberg blockade protocol, as explained in Section 1.2.2, was implemented, achieving a Bell state fidelity of $F_{\text{Bell}} = 0.59$.
In 2019, a significant improvement was made, reaching a Bell state fidelity of $F_{\text{Bell}} = 0.86$ [47].

Chapter 4

Qubits measurement and local gates

Now that we have defined the two-qubit system, and its CNOT gate, we need to think about how its state can be measured. Measurement is what bridges the microscopic, quantum world of the qubit to our macroscopic world. At first sight, the act of measuring may seem a rather straightforward task but it certainly is not. Some of the "strange" properties of quantum mechanics emerge from how quantum objects behave when measured. The measurement causes the collapse of the wavefunction of the quantum system and therefore the losse of information. In this part, one type of measurement, a projective measurement will be explained, and simulated including relaxation processes. This section will address measurements in the situation where the qubits are built without dressing the $3d_{3/2}$ state with the $4p_{1/2}$ state; however, the process remains the same for the situation with dressing.

Subsequently, single-qubit gates will be examined, with an explanation and simulation of the method for implementing a Z-gate on the Rydberg qubit. The objective is to establish a full set of gates that satisfy the criteria outlined by DiVincenzo and presented in Chapter 1.

4.1 Projective measurement

Theory

Projective measurement is characterized by an observable $\hat{M}$, a Hermitian operator on the state space of the system being measured. The observable can be

expressed through its spectral decomposition as:

$$\hat{M} = \sum_m m\hat{P}_m \tag{4.1}$$

where m represents the eigenvalues and $\hat{P}_m$ is the projector onto the eigenstate $|m\rangle$. The outcome of the measurement corresponds to one of the eigenvalues m of the observable. For the projective measurement of a qubit, it will projet the state on one of the two basis state of the qubit, $|0\rangle$ or $|1\rangle$. If the system is in an arbitrary state $|\psi\rangle$, the probability of obtaining the measurement result m is given by [48]:

$$p(m) = \langle\psi| \hat{P}_m |\psi\rangle \tag{4.2}$$

Following the measurement, the wavefunction collapses into the corresponding eigenstate. The post-measurement state is:

$$|\psi_m\rangle = \frac{\hat{P}_m |\psi\rangle}{\sqrt{p(m)}} \tag{4.3}$$

An important property of projective measurements is that once a measurement has been carried out, the outcome of a subsequent identical measurement is predetermined. This is because the state of the system collapses into one of the eigenstates of the observable after the first measurement, as demonstrated in [48]. Hence, any further measurement of the same observable will yield the same result, as the state of the system will remain unchanged.

Projective measurement on the core qubit

The measurement described here aims at obtaining information about the state of the Rydberg qubit using a projective measurement of the ion-core state $4s_{1/2}$, which corresponds to $|0\rangle$ for the core qubit, onto the state $4p_{1/2}$. This measurement is performed by coupling the $4s_{1/2}$ and $4p_{1/2}$ states with a resonant laser. If the $4s_{1/2}$ state is populated, meaning the core qubit state is $|0\rangle$, the population will oscillate between these two states at the Rabi frequency of 237.709 MHz (see Table 3.4). The populated $4p_{1/2}$ state will then induce radiative emission towards the $4s_{1/2}$ state with a emission coefficient $A_{4p_{1/2}\to 4s_{1/2}}$ of 1.4×10^8 s^{-1}, and also towards $3d_{3/2}$ with an emission coefficient $A_{4p_{1/2}\to 3d_{3/2}}$ of 1.06×10^7 s^{-1} [27]. These photon emissions can then be detected with appropriate instruments.

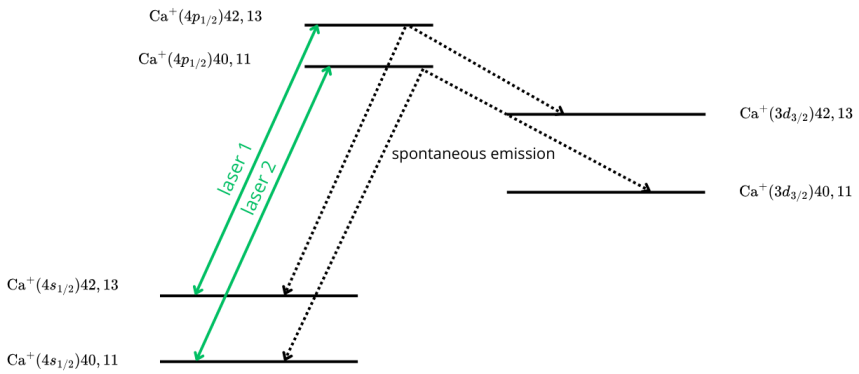

Figure 4.1 – Representation of the projective measurement on the core qubit. A resonant laser coupled states $Ca^+(4s_{1/2})n_2\ell_2$ and $Ca^+(4p_{1/2})n_2\ell_2$ to induce emission of photons (dotted lines) which can be detected.

These lasers must be resonant with the transition to optimize population transfer and photons emission. Therefore, we need to use two different lasers: one resonant laser for each Rydberg state, ensuring that there is always one resonant transition regardless of the Rydberg state.

Projective measurement on the Rydberg qubit

To perform a projective measurement on the Rydberg qubit, we initialize the core qubit in a known specific state and then perform a CNOT gate on the two-qubit system of the calcium atom. Assuming the state of the two individual qubits is given by

$$|\psi_{Rydberg}\rangle = \alpha\,|0\rangle + \beta\,|1\rangle\,, \tag{4.4}$$

$$|\psi_{core}\rangle = |1\rangle\,, \tag{4.5}$$

the wavefunction of the total system is then

$$|\psi\rangle = (\alpha\,|0\rangle + \beta\,|1\rangle) \otimes |1\rangle\,. \tag{4.6}$$

After the application of the CNOT gate, it becomes

$$|\psi\rangle = \alpha\,|01\rangle + \beta\,|10\rangle\,. \tag{4.7}$$

In this case, if after the application of the laser resonant with the transition between $4s_{1/2}$ and $4p_{1/2}$, we detect photons, it means that the core qubit state $|0\rangle$ is populated, and that the two-qubit system state is

$$|\psi\rangle = \beta\,|10\rangle\,. \tag{4.8}$$

The state of the Rydberg qubit is then:

$$|\psi_{Rydberg}\rangle = |1\rangle \,. \tag{4.9}$$

If no photon is detected after measuring the state obtained following the application of the CNOT gate (Equation (4.7)), it indicates that the core qubit state $|1\rangle$ is populated and that the two-qubit system is in the state

$$|\psi\rangle = \alpha\,|01\rangle \,. \tag{4.10}$$

The state of the Rydberg qubit is then:

$$|\psi_{Rydberg}\rangle = |0\rangle \,. \tag{4.11}$$

By repeating this projective measurement multiple times, it is possible to determine the values of the superposition coefficients α and β, as well as the initial state of the Rydberg qubit, except for the phase of the initial coherent superposition, without destroying the state. It is important to note that current methods for measuring Rydberg qubits typically involve destroying their state through field ionization [9].

The measurement described above is simulated below for the specific case where the two-qubit state before the CNOT gate is $|11\rangle$. The evolution of populations during and after the application of the CNOT gate is simulated in Figure 4.2, the period when the laser is turned off before the measurement, and after the CNOT gate is equal in duration to the CNOT operation.

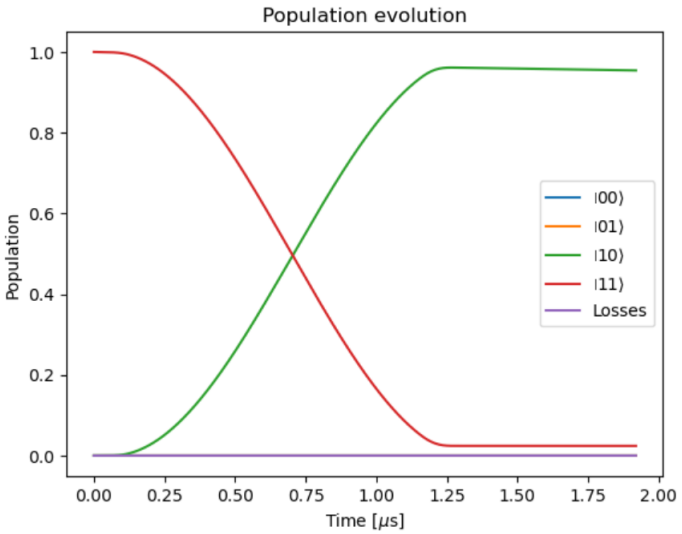

Figure 4.2 – Evolution of the population of the two-qubit state during the CNOT gate application and after the laser is turned off. The initial qubit states are $|1\rangle$ for both the Rydberg and core qubits.

Afterwards, the measurement is performed with a laser resonant between the states $Ca^+(4s_{1/2})42, 13$ and $Ca^+(4p_{1/2})42, 13$ ("laser 2" in Figure 4.2) which induces Rabi oscillations in these two populations, evolving over time as shown in Figure 4.3. The amplitude of the oscillations is progressively dampened due to the spontaneous emission from the $4p_{1/2}$ state to the $4s_{1/2}$ state. The frequency of these oscillations is high because of the large Rabi frequency for this dipole transition (≈ 237.709MHz), compared to the one of the quadrupole transition $4s_{1/2} \leftrightarrow 3d_{3/2}$ (≈ 0.391MHz).

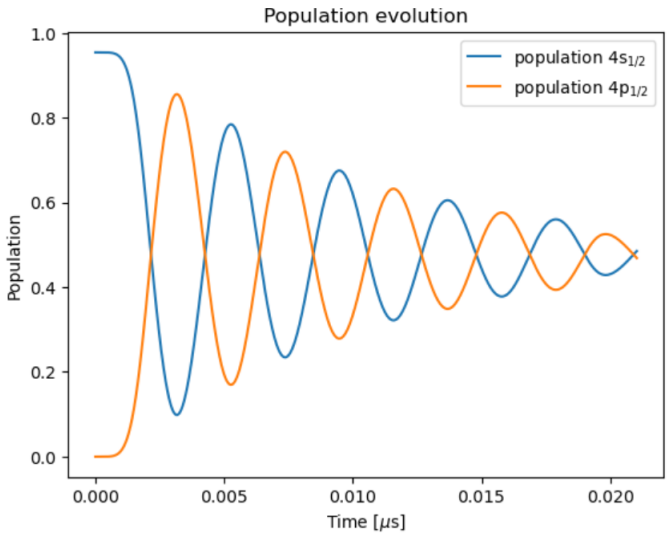

Figure 4.3 – Evolution of the population of states $4s_{1/2}$ and $4p_{1/2}$ after applying a laser resonant between these states. The population of the $4s_{1/2}$ state is that obtained after the operations shown in Figure 4.2. The rise and fall times of the laser pulse amplitude correspond to 1/10 of the pulse duration (2.1 ns)

The radiative emission of an electron from one state to another occurs at a rate A. This rate determines τ, the number of photons emitted per second, which is given by:

$$\tau = \sum_i A_i \rho_{ii}, \tag{4.12}$$

where the sum runs over the excited states i, with their populations ρ_{ii}. In our situation, this is solely the $4p_{1/2}$ state, with its radiative emission possible towards the $4s_{1/2}$ and $3d_{3/2}$ states.

Thus, the cumulative number of photons emitted after the application of the laser can be determined by integrating this over time. Finally, we can determine that the laser coupling states $4s_{1/2}$ and $4p_{1/2}$ should be turned on for at least $\approx$0.017 µs in order to detect one photon. The result is illustrated in Figure 4.4.

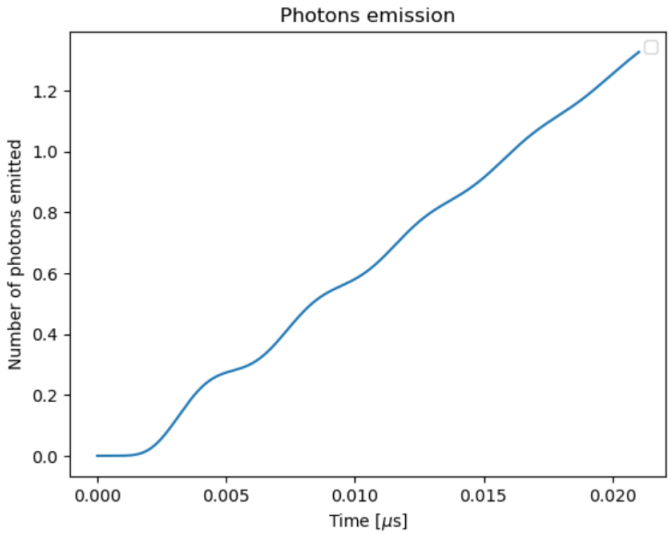

Figure 4.4 – Number of photons emitted after the application of a resonant laser between states $4s_{1/2}$ and $4p_{1/2}$ for the system state obtained after the projective measurement protocol described above.

4.2 Single-qubit gates

4.2.1 Single-qubit gates fundamentals

When addressing single-qubit gates on Rydberg qubits, a significant challenge is to achieve local manipulations rather than global ones, where global manipulations affect multiple qubits simultaneously. The energy difference between neighboring Rydberg states typically falls within the microwave range, with differences on the order of 0.3-300 GHz, corresponding to wavelengths of approximately 1-1000 mm. The close proximity of qubits relative to these large wavelengths can lead to complications [9].
However, single Rydberg qubit operations with minimal impact on neighboring qubits (low crosstalk) have been experimentally demonstrated. One approach involves using tightly focused lasers to produce local AC Stark shifts for addressing specific qubits in combination with global microwave couplings [49]. Another promising approach is described in [50], where the electrostatic coupling between the two valence electrons of strontium is used to manipulate a circular Rydberg state with optical pulses on the valence electron near the core. The shift resulting from the electrostatic interaction between the two valence electrons allows the state of the ionic core electron to be conditioned on the value n of the Rydberg qubit, thereby enabling its manipulation.

Single-qubit gate on ground-ground qubits (see Chapter 1) can be performed using optical lasers, which are well-developed and widely available. These lasers typically operate at optical frequencies, with energy differences between states around 400 THz.

To perform a single-qubit gate on either of our two qubits, different lasers are required to drive the transition, depending on the state of the other qubit. The energy shift resulting from the interaction between valence electrons causes a difference in the energy of the single-qubit transition $|0\rangle \leftrightarrow |1\rangle$, depending on the state of the other qubit. A representation of the single-qubit state transitions for our two-qubit system is shown in Figure 4.5.

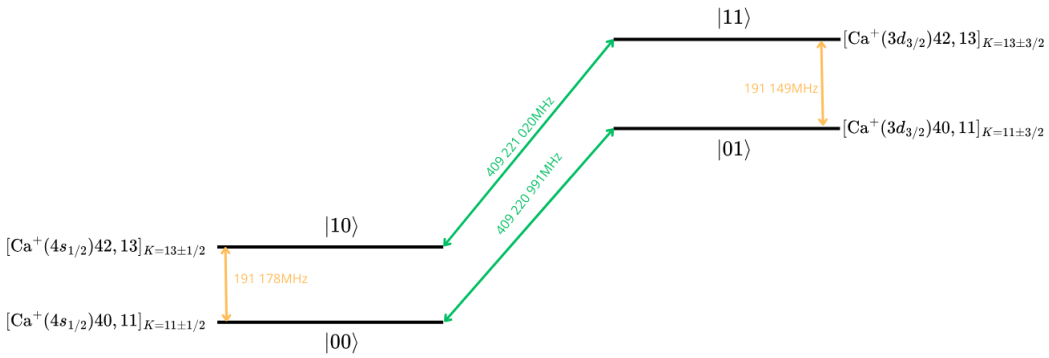

Figure 4.5 – Single-qubit transitions are represented as $|00\rangle \leftrightarrow |01\rangle$ and $|10\rangle \leftrightarrow |11\rangle$ for the core qubit (green arrows), and $|00\rangle \leftrightarrow |10\rangle$ and $|01\rangle \leftrightarrow |11\rangle$ for the Rydberg qubit (yellow arrows).

4.2.2 Local Z-gate for the Rydberg qubit

This section outlines how to execute a single-qubit Z gate (Pauli-Z gate) on the Rydberg qubit. This gate, also known as the phase-flip gate, leaves the basis state $|0\rangle$ unchanged and maps $|1\rangle$ to $-|1\rangle$.

Assume that the two qubits are in states

$$|\psi_{Rydberg}\rangle = \alpha\,|0\rangle + \beta\,|1\rangle\,, \tag{4.13}$$

$$|\psi_{core}\rangle = |0\rangle\,. \tag{4.14}$$

The wavefunction of the total system is then

$$|\psi\rangle = (\alpha\,|0\rangle + \beta\,|1\rangle) \otimes |0\rangle\,. \tag{4.15}$$

After the application of the CNOT gate, it becomes

$$|\psi\rangle = \alpha\,|00\rangle + \beta\,|11\rangle\,. \tag{4.16}$$

Applying a Hadamard gate with a $\pi/2$ pulse on the core qubit yields:

$$|\psi\rangle = \frac{1}{\sqrt{2}}(\alpha\,|0\rangle \otimes [|0\rangle + |1\rangle] + \beta\,|1\rangle \otimes [|0\rangle - |1\rangle]), \tag{4.17}$$

which can be rewritten as, showing the superposition of the four basis states of the two-qubit system:

$$|\psi\rangle = \frac{1}{\sqrt{2}}(\alpha\,|00\rangle + \alpha\,|01\rangle + \beta\,|10\rangle - \beta\,|11\rangle). \tag{4.18}$$

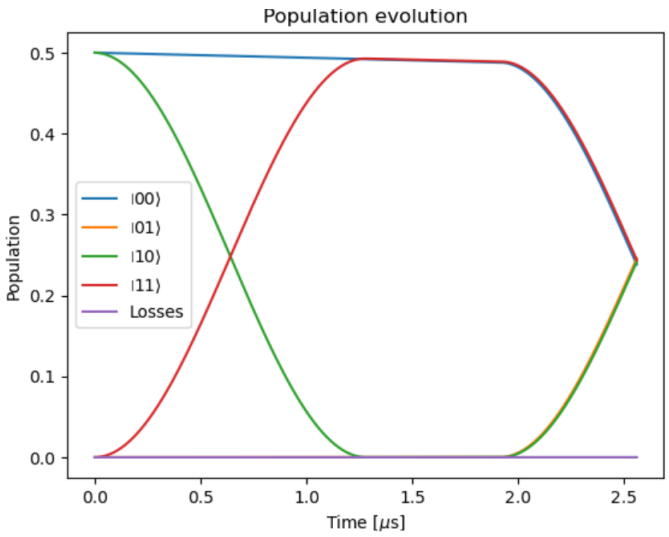

Figure 4.6 – Evolution of the population of two-qubit states during the CNOT gate application and the $\pi/2$-pulse performed on the core-qubit afterwards, starting with the two-qubit state $\frac{1}{\sqrt{2}}(|00\rangle + |10\rangle)$

A projective measurement on the core qubit can then be performed using a laser coupled between the $4s_{1/2}$ and $4p_{1/2}$ states, as described in the Section 4.1. This measurement causes the core qubit's state to collapse to either $|0\rangle$ or $|1\rangle$. To illustrate the two possible outcomes for the core qubit, we rewrite Equation (4.18) to expose core qubit state as follows:

$$|\psi\rangle = \frac{1}{\sqrt{2}}\left([\alpha\,|0\rangle + \beta\,|1\rangle] \otimes |0\rangle + [\alpha\,|0\rangle - \beta\,|1\rangle] \otimes |1\rangle\right), \tag{4.19}$$

Therefore, based on whether photons are detected, as illustrated in Figure 4.7, we can determine if a Z-gate has been performed on the Rydberg qubit. This process does not destroy the superposition state of the Rydberg qubit.

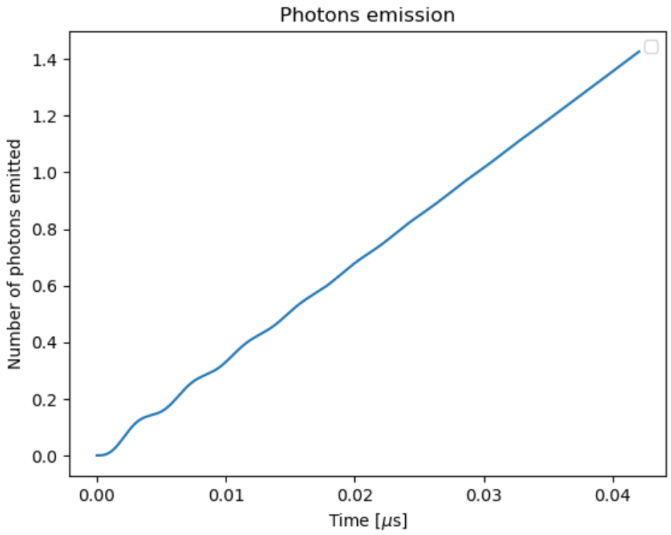

Figure 4.7 – Number of photons emitted after the application of a resonant laser between states $4s_{1/2}$ and $4p_{1/2}$ for the system state obtained after a CNOT gate followed by a $\pi/2$ pulse on the core qubit, starting with the two-qubit state $\frac{1}{\sqrt{2}}(|00\rangle + |10\rangle)$

In the end, starting with the core qubit in the state $|0\rangle$ and the Rydberg qubit in an unknown superposition state, we successfully performed a local gate on our two-qubit system: a Z-gate on the Rydberg qubit, which is uncommon for Rydberg-Rydberg qubits [9].

Conclusion

In this thesis, we have investigated the use of two valence electrons in calcium Rydberg atoms to explore the potential for implementing an architecture that incorporates two qubits within a single atom. The primary focus was on simulating a Controlled-NOT (CNOT) gate using these two qubits, laying the groundwork for a quantum system capable of performing quantum computing and simulations.

After a review of the theoretical background in Rydberg atom physics, including valence electron interactions, the research began with a detailed description of the two-qubit architecture within a calcium Rydberg atom. This involved selecting appropriate electronic levels, calculating energy shifts (with the aid of [25]), and discussing the results to determine the optimal levels for qubit operations. The main factors guiding the choice were the state lifetime, which affects decoherence, and the state energy shift, to fulfill the requirements needed for the CNOT gate. Ultimately, the core qubit basis states $|0\rangle$ and $|1\rangle$ were chosen to be $\left|\mathrm{Ca}^{+}(4\mathrm{s}_{1/2})\right\rangle$ and $\left|\mathrm{Ca}^{+}(3\mathrm{d}_{3/2})\right\rangle$, respectively. Regarding the Rydberg qubit, the selected states for the Rydberg qubit basis states $|0\rangle$ and $|1\rangle$ were described by their quantum numbers n and ℓ: $|n = 40, \ell = 11\rangle$ and $|n = 42, \ell = 13\rangle$, respectively.
Subsequently, another architecture was explored with the aim of improving the speed of the CNOT gate. This involved replacing the core qubit basis state $|1\rangle$ with a dressed state, specifically dressing $\left|\mathrm{Ca}^{+}(3\mathrm{d}_{3/2})\right\rangle$ with $\left|\mathrm{Ca}^{+}(4\mathrm{p}_{1/2})\right\rangle$.

The simulation of the CNOT gate was performed by constructing the Hamiltonian of the system, incorporating interactions with a laser pulse to execute the gate. For this purpose, the Rabi frequencies of dipole and quadrupole electronic transitions were calculated. To evaluate the gate performance over time, we accounted for the impact of incoherent relaxation processes of qubit states such as autoionization, spontaneous emission, and Rydberg state decay. The various relaxation rates were estimated using analytical formulas and existing literature, including [29], and were integrated into the simulation.

The evolution of the quantum system under the action of the laser pulse used

to perform the CNOT gate was simulated, revealing the dynamics of the qubits during gate operation. We demonstrated that it is possible to operate a CNOT gate with the core qubit as the target and the Rydberg qubit as the control on a timescale of approximately 1 μs and with high fidelity. The comparison between the architecture with and without dressing was particularly insightful. On one hand, the gate duration was significantly reduced from 1.279 μs to 0.510 μs. On the other hand, it was observed that decoherence in some two-qubit states was significantly impacted by the dressing, leading to a decrease in gate fidelity. For instance, the fidelity for the state $|01\rangle$ decreased from 0.992 to 0.905. The excellent fidelity for the undressed state, combined with the reasonable timescale for gate operation, could be experimentally tested in the near future. The main limitation to the fidelity of this architecture is black body radiation-induced transitions, which could be mitigated by lowering the temperature of the environment surrounding the atoms to cryogenic levels. Another possibility is to shield the atoms from microwave radiation [43].

We also examined projective measurement on both qubits. The core qubit measurement is performed using a laser that couples the ion-core states $Ca^+(4s_{1/2})$ and $Ca^+(4p_{1/2})$, while the measured state is determined by detecting photons emitted from the radiative decay of $Ca^+(4p_{1/2})$. A method to measure the Rydberg qubit state is described, which uses a projective measurement on the core qubit and does not collapse the superposition of the Rydberg qubit state. Additionally, we investigated single-qubit operations for our two-qubit system and proposed a method to perform a local Z-gate on the Rydberg qubit, which is uncommon for Rydberg-Rydberg qubits [9].

The results presented in this thesis are promising and demonstrate the theoretical feasibility of an innovative qubit architecture. A key area for future work is the experimental validation of the simulated CNOT gate. Implementing this setup in a laboratory setting would provide valuable insights into practical challenges and limitations that may not be fully captured by simulations. However, before moving to experimental implementation, several additional aspects should be considered. Firstly, the theoretical simulation of this qubit architecture could be improved by incorporating individual K-levels arising from the jK coupling between valence electrons. Additionally, the pulse simulation included in this work should be refined to account for realistic linewidths, as the frequency dispersion of the laser pulse was not considered. The method for driving the forbidden transition between the $4s_{1/2}$ and $3d_{3/2}$ states should also be further investigated, as a two-photon Raman transition may provide a more effective approach.
Finally, investigating the interactions between multiple Rydberg atoms could lead

to the development of more complex quantum gates and entanglement protocols. Currently, our system is limited to two qubits, which is insufficient for quantum computation. Extending this architecture to include multiple atoms is a necessary step, for which preliminary work was initiated but not fully developed due to time constraints. A preliminary literature review on the interactions between Rydberg atoms is included as an Appendix for future reference. These enhancements are crucial for advancing this qubit system and could make a significant contribution to the promising field of quantum computing.

Appendix A

Multiple atoms system

A.1 Introduction

In order to develop a robust qubit system capable of supporting a large number of operations, it is essential to use multiple calcium atoms, in our situation each containing two qubits, in close proximity. The scalability and performance of such a quantum system can also be significantly enhanced by creating entanglement among more than two qubits, such as through GHZ entanglement [48]. This requires a deep understanding of the interactions between different calcium Rydberg atoms.

In this work, we provide an introductory overview of the potential methods for studying and leveraging these interactions. By exploring the fundamental principles and potential techniques, we aim to lay the groundwork for future research and development in this promising area of quantum computing.

A.2 Rydberg-Rydberg interactions

One consequence of the large dipole moment featured by Rydberg atoms is the significant interaction between two of them. Let us consider two atoms, A and B, separated by a distance R. These two atoms predominantly interact via a dipole-dipole coupling, described by [9]:

$$\hat{V} = \frac{1}{4\pi\epsilon_0 R^3}\left(\hat{\mathbf{d}}_A \cdot \hat{\mathbf{d}}_B - 3(\hat{\mathbf{d}}_A \cdot \hat{\mathbf{r}})(\hat{\mathbf{d}}_B \cdot \hat{\mathbf{r}})\right), \tag{A.1}$$

where $\hat{\mathbf{r}} = \mathbf{R}/R$ is the unit vector linking the two atoms, and $\hat{\mathbf{d}}_A$ and $\hat{\mathbf{d}}_B$ are the electric dipole operators for atoms A and B, respectively. The Hamiltonian of this interaction acts on the two-atom basis.

Let us consider one pair of dipole-coupled states for each atom, with a similar energy difference between them. Respectively, for atoms A and B, the dipole-coupled pairs are:

$$|n_A \ell_A\rangle \longleftrightarrow |n'_A \ell'_A\rangle \,, \tag{A.2}$$

$$|n_B \ell_B\rangle \longleftrightarrow |n'_B \ell'_B\rangle \,. \tag{A.3}$$

For simplicity, we neglect the angular dependence in Equation (A.1) of the dipole-dipole interaction. Let us assume that the two atoms are in the states $|n_A \ell_A\rangle$ and $|n_B \ell_B\rangle$, thus our two-atom system is in the configuration $|n_A \ell_A\rangle \otimes |n_B \ell_B\rangle$. Often, the coupling by $\hat{V}$ of this two-atom state to other two-atom states is dominated by the coupling to only one other two-atom state, and the two-atom system can then be reduced to an effective two-level system.
In this case, the Hamiltonian of the two atoms, reduced to the $\{|n_A \ell_A n_B \ell_B\rangle \,, |n'_A \ell'_A n'_B \ell'_B\rangle\}$ pair state basis, is:

$$\hat{H} = \begin{pmatrix} 0 & C_3/R^3 \\ C_3/R^3 & \Delta_F \end{pmatrix} , \tag{A.4}$$

with $C_3/R^3 = \langle n_A \ell_A n_B \ell_B | \, \hat{V} \, | n'_A \ell'_A n'_B \ell'_B \rangle$ and the so-called Förster defect Δ_F, is:

$$\Delta_F = \delta = E_{n_A \ell_A} + E_{n_B \ell_B} - (E_{n'_A \ell'_A} + E_{n'_B \ell'_B}). \tag{A.5}$$

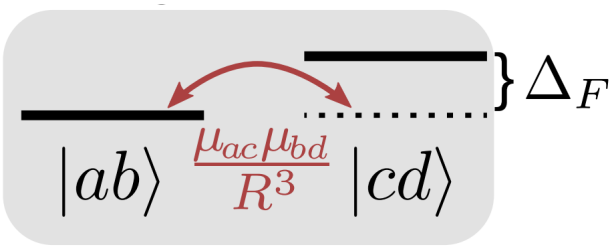

Figure A.1 – Interaction between two Rydberg atoms, with the two-atom states represented as $|ab\rangle = |n_A \ell_A n_B \ell_B\rangle$ and $|cd\rangle = |n'_A \ell'_A n'_B \ell'_B\rangle$. Image taken from [9].

The eigenenergies of this Hamiltonian are:

$$\Delta E_{\pm} = \frac{\Delta_F}{2} \pm \frac{1}{2}\sqrt{\Delta_F^2 + \left(\frac{C_3}{R^3}\right)^2}. \tag{A.6}$$

Based on the magnitude of the Förster defect Δ_F, two distinct interaction regimes can be identified, depending on the inter-atomic distance R. The transition between

these regimes occurs when the dipole-dipole interaction energy $V(R)$ equals the Förster defect Δ_F. This specific inter-atomic distance is referred to as the Van der Waals radius. The details of these regimes are explained below.

Resonant interactions ($\Delta_F << C_3/R^3$)

In this situation, with ($\Delta_F << C_3/R^3$), the eigenenergies of the Hamiltonian are [21]:

$$\Delta E_{\pm} \approx \pm \frac{C_3}{R^3}, \tag{A.7}$$

with C_3 scaling as $\propto n^4$. In this situation, there is a coherent exchange process between the two two-atom states, taking the form:

$$|\pm\rangle = \frac{1}{\sqrt{2}}(|n_A \ell_A n_B \ell_B\rangle \mp |n'_A \ell'_A n'_B \ell'_B\rangle). \tag{A.8}$$

In the resonant regime, it is possible to set $\Delta_F = 0$ by exploiting the DC-Stark shift, applying an external electric field which shifts the levels $|n_A \ell_A n_B \ell_B\rangle$ and $|n'_A \ell'_A n'_B \ell'_B\rangle$ relative to each other to achieve zero energy difference. In this case, the interaction energy scales as $\propto 1/R^3$ regardless of the distance between the two atoms. This phenomenon is known as Förster resonance.

In the situation described in this work, where two calcium Rydberg atoms each contain two qubits as outlined in the previous chapters, the energy difference between highly excited Rydberg states is very small. Consequently, $\Delta_F \ll C_3/R^3$, indicating that the system is in a situation of Förster resonance, while the inter-atomic distance keeps small.

Non-resonant interactions($\Delta_F >> C_3/R^3$)

In the large R limit, the interaction between Rydberg atoms is typically dominated by dipole-dipole interactions. This interaction couples an initial two-atom state $|n_A \ell_A n_B \ell_B\rangle$ to other states $|n'_A \ell'_A n'_B \ell'_B\rangle$, where the energy difference is given by the Förster defect $\Delta_{n'_A \ell'_A n'_B \ell'_B} = E_{n'_A \ell'_A} + E_{n'_B \ell'_B} - E_{n_A \ell_A} - E_{n_B \ell_B}$.

In the case where $\Delta_F \gg C_3/R^3$, the two two-atom states are weakly mixed, and the primary effect of this interaction is to shift the energy of the two-atom state $|n_A \ell_A n_B \ell_B\rangle$ by [21]:

$$\Delta E_{-} \approx \frac{1}{\Delta_F} \left(\frac{C_3}{R^3}\right)^2. \tag{A.9}$$

This corresponds to the Van der Waals limit, where the energy shift of the initial state scales as $\propto C_6/R^6$, with a dependence on $\propto n^{11}$. This scaling is derived from $C_3 \propto d^2 \propto n^4$ and $\Delta_F \propto 1/n^3$, yielding $\propto n^{11}$.

Theoretically, the energy shift of the two-atom state $|n\ell, n\ell\rangle$, accounting for the contributions from all dipole-coupled states, can be calculated using second-order perturbation theory as:

$$\Delta E_{n\ell,n\ell} = \sum_{n'\ell',n''\ell''} \frac{|\langle n\ell, n\ell|\hat{V}|n'\ell', n''\ell''\rangle|^2}{2E_{n\ell} - E_{n'\ell'} - E_{n''\ell''}}, \tag{A.10}$$

where the sum runs over all the two-atom $|n'\ell' n''\ell''\rangle$ states that are dipole-coupled to the original pair $|n\ell, n\ell\rangle$.

Use of artificial intelligence

In this work, I utilized artificial intelligence during the writing phase to correct and occasionally rephrase my sentences. Since English is not my native language, this assistance enabled me to provide more refined explanations. At no point did the ideas come from AI, all thoughts and concepts were my own. The role of AI was limited to correcting grammar and spelling, and sometimes suggesting more accurate synonyms. The AI tool I used for this task was ChatGPT from OpenAI [51].

Bibliography

[1] World Economic Forum. Explainer: What is quantum technology?, 2024. Accessed: 2024-08-07.

[2] MarketsandMarkets. Quantum computing market, 2024. Accessed: 2024-08-07.

[3] T.H. Johnson, S.R. Clark, and D. Jaksch. What is a quantum simulator? *EPJ Quantum Technology*, 1:10, 2014.

[4] Jian-Qiang You and Franco Nori. Atomic physics and quantum optics using superconducting circuits. *Nature*, 474(7353):589–597, 2011.

[5] Ivan Kassal, James D Whitfield, Alejandro Perdomo-Ortiz, Man-Hong Yung, and Alán Aspuru-Guzik. Simulating chemistry using quantum computers. *Annual review of physical chemistry*, 62(1):185–207, 2011.

[6] Stephen P Jordan, Keith SM Lee, and John Preskill. Quantum algorithms for quantum field theories. *Science*, 336(6085):1130–1133, 2012.

[7] David P. DiVincenzo. The physical implementation of quantum computation. *Fortschritte der Physik*, 48(9–11):771–783, September 2000.

[8] Rydberg Technologies. Rydberg technologies. `https://www.rydbergtechnologies.com/`. Accessed: 2024-07-31.

[9] M. Morgado and S. Whitlock. Quantum simulation and computing with rydberg-interacting qubits. *AVS Quantum Science*, 3(2), May 2021.

[10] Bilal Sheik. Quantum 101: What is a Qubit (quantum bits)?, February 2024.

[11] Alain Aspect, Jean Dalibard, and Gérard Roger. Experimental test of bell's inequalities using time-varying analyzers. *Phys. Rev. Lett.*, 49:1804–1807, Dec 1982.

[12] Qiskit. How The First Superconducting Qubit Changed Quantum Computing Forever, September 2022.

[13] He-Liang Huang, Dachao Wu, Daojin Fan, and Xiaobo Zhu. Superconducting quantum computing: a review. *Science China Information Sciences*, 63(8), July 2020.

[14] Colin D Bruzewicz, John Chiaverini, Robert McConnell, and Jeremy M Sage. Trapped-ion quantum computing: Progress and challenges. *Applied Physics Reviews*, 6(2), 2019.

[15] Adam M Kaufman, Brian J Lester, and Cindy A Regal. Cooling a single atom in an optical tweezer to its quantum ground state. *Physical Review X*, 2(4):041014, 2012.

[16] Wikipedia contributors. Church–turing thesis — Wikipedia, the free encyclopedia. `https://en.wikipedia.org/w/index.php?title=Church%E2%80%93Turing_thesis&oldid=1215851602`, 2024. [Online; accessed 25-May-2024].

[17] Randall G. Hulet and Daniel Kleppner. Rydberg atoms in "circular" states. *Phys. Rev. Lett.*, 51:1430–1433, Oct 1983.

[18] Thomas F. Gallagher. *Rydberg Atoms*. Cambridge Monographs on Atomic, Molecular and Chemical Physics. Cambridge University Press, 1994.

[19] F. Barry Dunning and Thomas C. Killian. Rydberg Atoms: Giants of the Atomic World. *Scientia*, 2021.

[20] D. Tong, S. M. Farooqi, J. Stanojevic, S. Krishnan, Y. P. Zhang, R. Côté, E. E. Eyler, and P. L. Gould. Local blockade of rydberg excitation in an ultracold gas. *Phys. Rev. Lett.*, 93:063001, Aug 2004.

[21] Antoine Browaeys and Thierry Lahaye. *Interacting Cold Rydberg Atoms: A Toy Many-Body System*, pages 177–198. Springer International Publishing, Cham, 2016.

[22] E. Urban, T. A. Johnson, T. Henage, L. Isenhower, D. D. Yavuz, T. G. Walker, and M. Saffman. Observation of Rydberg blockade between two atoms. *Nature Phys.*, 5(2):110–114, 2009.

[23] M. Saffman, T. G. Walker, and K. Mølmer. Quantum information with rydberg atoms. *Reviews of Modern Physics*, 82(3):2313–2363, August 2010.

[24] H. Wu, R. Richaud, J.-M. Raimond, M. Brune, and S. Gleyzes. Millisecond-lived circular rydberg atoms in a room-temperature experiment. *Phys. Rev. Lett.*, 130:023202, Jan 2023.

[25] Alisée Bouillon. *Theory of Rydberg-Atom Laser Cooling by Isolated Core Excitation*. PhD thesis, UCL - Faculté des sciences, 2023.

[26] Elaine R. Stearney, Julian A. Jakubowski, and Angela C. Regina. Beryllium Toxicity. In *StatPearls*. StatPearls Publishing, Treasure Island (FL), 2024.

[27] Alexander Kramida and Yuri Ralchenko. NIST Atomic Spectra Database, NIST Standard Reference Database 78, 1999.

[28] S. A. Bhatti, C. L. Cromer, and W. E. Cooke. Analysis of the rydberg character of the $5d7d^1d_2$ state of barium. *Phys. Rev. A*, 24:161–165, Jul 1981.

[29] Dominik Wehrli, Matthieu Génévriez, and Frédéric Merkt. Autoionization rates of core-excited magnesium rydberg atoms in electric fields using the core fluorescence as a reference. *Physical Review A*, 2019.

[30] Henri Lehec. *Spectroscopie Rydberg et excitation du coeur isolé d'atomes d'ytterbium ultra-froids*. PhD thesis, 2017. Thèse de doctorat dirigée par Pillet, Pierre Physique quantique Université Paris-Saclay (ComUE) 2017.

[31] R. Blatt, Hartmut Haeffner, Christian Roos, Christoph Becher, and Ferdinand Schmidt-Kaler. *Ion Trap Quantum Computing with Ca+ Ions*, volume 3, pages 61–73. 01 2005.

[32] Robert D. Cowan. *The Theory of Atomic Structure and Spectra*. University of California Press, Berkeley, 1981.

[33] Constantine Theodosiou. Accurate calculation of the 4p lifetimes of ca+. *Physical review. A*, 39:4880–4883, 06 1989.

[34] P. A. Barton, C. J. S. Donald, D. M. Lucas, D. A. Stevens, A. M. Steane, and D. N. Stacey. Measurement of the lifetime of the $3d^2D_{5/2}$ state in $^{40}ca^+$. *Phys. Rev. A*, 62:032503, Aug 2000.

[35] E. Marin-Bujedo and M. Génévriez. Autoionization of high- core-excited rydberg states of alkaline-earth-metal atoms. *Physical Review A*, 108(1), July 2023.

[36] J.R. Johansson, P.D. Nation, and Franco Nori. QuTiP 2: A python framework for the dynamics of open quantum systems. *Computer Physics Communications*, 184(4):1234–1240, apr 2013.

[37] Matthieu Génévriez and Clément Lauzin. Physique atomique et moléculaire. `https://uclouvain.be/cours-2023-LPHYS1344.html`, 2024. Université catholique de Louvain, 5.00 crédits, 22.5 h + 22.5 h Q2.

[38] J. Mitroy and J.-Y Zhang. Long range interactions of the mg+ and ca+ ions. *European Physical Journal D*, 46:415–424, 03 2008.

[39] A. D. Bounds, N. C. Jackson, R. K. Hanley, R. Faoro, E. M. Bridge, P. Huillery, and M. P. A. Jones. Rydberg-dressed magneto-optical trap. *Phys. Rev. Lett.*, 120:183401, May 2018.

[40] Gilbert Grynberg, Alain Aspect, and Claude Fabre. *Frontmatter*, page i–vii. Cambridge University Press, 2010.

[41] E. Marin-Bujedo and M. Génévriez. Autoionization of high-l core-excited rydberg states of alkaline-earth-metal atoms. *Physical Review A*, 108(1), July 2023.

[42] Lindblad Master Equation Solver — QuTiP 4.0 Documentation.

[43] H. Wu, R. Richaud, J.-M. Raimond, M. Brune, and S. Gleyzes. Millisecond-lived circular rydberg atoms in a room-temperature experiment. *Physical Review Letters*, 130(2), January 2023.

[44] Michael A. Nielsen and Isaac L. Chuang. *Quantum Computation and Quantum Information: 10th Anniversary Edition*. Cambridge University Press, 2010.

[45] L. Isenhower, E. Urban, X. L. Zhang, A. T. Gill, T. Henage, T. A. Johnson, T. G. Walker, and M. Saffman. Demonstration of a neutral atom controlled-not quantum gate. *Physical Review Letters*, 104(1), January 2010.

[46] Yong Zeng, Peng Xu, Xiaodong He, Yangyang Liu, Min Liu, Jin Wang, D. J. Papoular, G. V. Shlyapnikov, and Mingsheng Zhan. Entangling two individual atoms of different isotopes via rydberg blockade. *Phys. Rev. Lett.*, 119:160502, Oct 2017.

[47] T.M. Graham, M. Kwon, B. Grinkemeyer, Z. Marra, X. Jiang, M.T. Lichtman, Y. Sun, M. Ebert, and M. Saffman. Rydberg-mediated entanglement in a two-dimensional neutral atom qubit array. *Physical Review Letters*, 123(23), December 2019.

[48] Matthieu Génévriez. Lphys2242: Fundamentals of quantum information. `https://uclouvain.be/cours-2023-LPHYS2242.html`, May 2023. Lecture slides.

[49] T. M. Graham, M. Kwon, B. Grinkemeyer, Z. Marra, X. Jiang, M. T. Lichtman, Y. Sun, M. Ebert, and M. Saffman. Rydberg-mediated entanglement in a two-dimensional neutral atom qubit array. *Phys. Rev. Lett.*, 123:230501, Dec 2019.

[50] Andrea Muni, Léa Lachaud, Angelo Couto, Michel Poirier, Raul Celistrino Teixeira, Jean-Michel Raimond, Michel Brune, and Sébastien Gleyzes. Optical coherent manipulation of alkaline-earth circular rydberg states. *Nature Physics*, 18(5):502–505, March 2022.

[51] OpenAI. Chatgpt. `https://www.openai.com/chatgpt`, 2024.

UNIVERSITÉ CATHOLIQUE DE LOUVAIN
École polytechnique de Louvain
Rue Archimède, 1 bte L6.11.01, 1348 Louvain-la-Neuve, Belgique | **www.uclouvain.be/epl**